BIOCHEMISTRY

Assessing cancer therapeutic efficacy in vivo using [$^2H_7$] glucose deuterium metabolic imaging

Mario C. Chang[1], Vinay R. Malut[1], Rohit Mahar[2], Anna Rushin[1], Marc A. McLeod[3], Geraldine L. Pierre[1], Indu R. Malut[1], Stephen J. Staklinski[4], Max E. Glanz[1], Mukundan Ragavan[5], Gaurav Sharma[1], Manoj Madheswaran[1], Arshee Badar[1], Aparna D. Rao[6,7], Brian K. Law[8], Michael S. Kilberg[1], James H. P. Collins[9], Vikram D. Kodibagkar[10], James A. Bankson[11], Ralph J. DeBerardinis[3,12,13], Matthew E. Merritt[1]*

Metabolic imaging produces powerful visual assessments of organ function in vivo. Current techniques can be improved by safely increasing metabolic contrast. The gold standard, 2-[^{18}F]fluorodeoxyglucose-positron emission tomography (FDG-PET) imaging, is limited by radioactive exposure and sparse assessment of metabolism beyond glucose uptake and retention. Deuterium magnetic resonance imaging (DMRI) with [6,6-$^2H_2$]glucose is nonradioactive, achieves tumor metabolic contrast, but can be improved by enriched contrast from deuterated water (HDO) based imaging. Here, we developed a DMRI protocol employing [$^2H_7$]glucose. Imaging ^{2}H-signal and measuring HDO production in tumor-bearing mice detected differential glucose utilization across baseline tumors, tumors treated with vehicle control or anti-glycolytic BRAFi and MEKi therapy, and contralateral healthy tissue. Control tumors generated the most ^{2}H-signal and HDO. To our knowledge this is the first application of DMRI with [$^2H_7$]glucose for tumoral treatment monitoring. This approach demonstrates HDO as a marker of tumor glucose utilization and suggests translational capability in humans due to its safety, noninvasiveness, and suitability for serial monitoring.

INTRODUCTION

Cancer is the second leading cause of death behind heart disease (*1*). Although substantial improvements have been made in cancer therapeutics, early detection and treatment monitoring are essential for increasing overall patient survival rates. Furthermore, traditional cancer diagnostics such as biopsies and laboratory assessments are limited by sampling bias or by insufficient sensitivity and specificity required for complete diagnosis, posing a notable confounder for patient health (*2*, *3*). There remains a pressing need for improved cancer diagnostics for patient care. One of the primary diagnostic methodologies is in vivo imaging, which is the only technique that allows for an internal assessment of cancer when physical examination is not a suitable alternative (*4*). In particular, metabolic imaging is a powerful modality that allows for a direct visual assessment of real-time tumor metabolism in the human body. Present imaging techniques can be improved through the development of safe and noninvasive metabolic contrast approaches. ^{1}H magnetic resonance spectroscopic imaging (MRSI) is a robust approach that can generate tumoral contrast by imaging ^{1}H spectroscopy metabolite signals. ^{1}H MRSI has shown substantial promise in breast cancer cases where total choline is accumulated in sufficiently large levels that distinguish cancer from healthy tissue (*5*). The high abundance of hydrogen allows ^{1}H MRSI to acquire high SNR and resolution images but at the cost of specificity. However, without the use of an isotope tracer, there is no straightforward way of detecting the specific reactions that contribute to the generation of signal. The gold standard metabolic imaging technique for cancer detection and staging is 2-[^{18}F]fluorodeoxyglucose–positron emission tomography (FDG-PET) (*6*, *7*), which is performed about 2.2 million times per year in the United States (*8*, *9*). Although FDG-PET can detect the presence of many cancers with extremely high sensitivity, it is limited by the use of a radioactive glucose tracer that imposes a risk for secondary cancer, has limited serial monitoring capacity, and is sensitive to glucose uptake but not glycolytic utilization or downstream metabolism (*10*–*12*). In addition, FDG-PET methodology is less selective in tissues where glucose utilization is notably high (e.g., brain).

In contrast, deuterium magnetic resonance imaging (DMRI) can generate metabolic contrast without using ionizing radiation and has the ability to report both tracer uptake and labeling of downstream intermediates through metabolic activity within the tissue. The application of DMRI in human cancer was demonstrated by the seminal work of de Feyter *et al.* (*13*), in which a human glioblastoma was imaged with the detection of ^{2}H-lactate and ^{2}H-glutamine/glutamate (glx) generated from a [6,6′-$^2H_2$]glucose contrast agent. Given the safety of deuterated tracers along with the ability to generate distinct tumoral metabolic contrast within highly glycolytic

[1]Department of Biochemistry and Molecular Biology, University of Florida College of Medicine, Gainesville, FL 32610, USA. [2]Department of Chemistry, Hemvati Nandan Bahuguna Garhwal University (A Central University), Srinagar Garhwal, Uttarakhand 246174, India. [3]Center for Human Nutrition, University of Texas Southwestern Medical Center, Dallas, TX 75390, USA. [4]School of Biological Sciences, Cold Spring Harbor Laboratory, Cold Spring Harbor, NY 11724, USA. [5]Department of Structural Biology, St. Jude Children's Research Hospital, Memphis, TN 38105, USA. [6]Peter MacCallum Cancer Centre, Melbourne, Victoria 3000, Australia. [7]Sir Peter MacCallum Department of Oncology, The University of Melbourne, Parkville, Victoria 3010, Australia. [8]Department of Pharmacology and Therapeutics, University of Florida College of Medicine, Gainesville, FL, 32610, USA. [9]National High Magnetic Field Laboratory, University of Florida, Gainesville, FL 32610, USA. [10]School of Biological and Health Systems Engineering, Arizona State University, Tempe, AZ 85281, USA. [11]Department of Imaging Physics, The University of Texas MD Anderson Cancer Center, Houston, TX 77030, USA. [12]Howard Hughes Medical Institute, University of Texas Southwestern Medical Center, Dallas, TX 75390, USA. [13]Children's Medical Center Research Institute, University of Texas Southwestern Medical Center, Dallas, TX 75390, USA.
*Corresponding author. Email: matthewmerritt@ufl.edu

brain tissue, DMRI with [6,6′-$^2H_2$]glucose has potential as a clinical approach for detecting cancer metabolism. However, this method has limited sensitivity, resulting in long scan times. We hypothesized that [$^2H_7$]glucose might provide increased sensitivity. Unlike partially deuterated tracers such as [6,6′-$^2H_2$]glucose, perdeuterated [$^2H_7$]glucose generates significantly more HDO and greater MRI signal that can be used to improve spatial resolution. In combination with imaging an earlier time frame after the administration of [$^2H_7$]glucose, this methodology can use simple MRI sequences that are substantially faster than chemical shift imaging methods.

Most cancer cells consume more glucose and produce more lactate relative to nonmalignant cells (the Warburg effect) (*14*, *15*). By assessing differential glucose consumption, one can get a direct readout of metabolic activity in cancer. Therefore, with [$^2H_7$]glucose, we can assess glucose utilization by measuring the production of HDO in tumors with high sensitivity and specificity as well as in a safe and minimally invasive manner. Focusing on the initial kinetics and using [$^2H_7$]glucose, we can detect localized metabolism associated with the bioenergetics of glycolysis and, to some extent, mitochondrial respiration (*16*). We previously demonstrated that HDO production and [$^2H_7$]glucose consumption are positively and linearly correlated in cell culture models (*17*–*19*). Notably, HDO production was more sensitive to glycolytic flux than lactate, as lactate production and glucose consumption did not correlate well at early time points following tracer administration. In addition, HDO has a natural abundance (NA) of 0.015%, with a readily detectable signal before any deuterated tracer is metabolized. This makes HDO a more robust metric, as HDO generation can be measured as an overall increase from NA, while deuterated lactate and glx are initially undetectable. This circumstance allows HDO spectra and images to be acquired with higher initial signal-to-noise (SNR) than detection of lactate or glx. Using the endogenous NA HDO signal normalization is superior to the use of an external phantom, as there could be a voxel-by-voxel correction for osmolality and temperature that cannot be simulated with a single external standard in a straightforward manner.

To assess the in vivo potential of using HDO as a marker of glycolytic flux, we imaged glucose metabolism in the rat brain. With this murine model, we have shown that DMRI can track HDO production in a timely manner, with a highly conserved correlation between HDO and glx generation between 8 and 24 min after injection of [$^2H_7$]glucose (*18*). Notably, HDO maintained superior SNR in ^2H nuclear magnetic resonance (NMR) spectra compared to lactate and glx. Thus, HDO production is a logical in vivo biomarker for monitoring treatments that perturb glycolysis.

Here, we examine the ability of this method to detect metabolic responses arising from successful cancer therapy. We used Yale University Mouse Melanoma 1.7 (Yumm1.7) cells in culture and in subcutaneous xenografts. Yumm1.7 melanoma cells contain the common BRAF V600E mutation and express inactive Phosphatase and Tensin homolog (PTEN) and Cyclin-Dependent Kinase Inhibitor 2a (Cdkn2a), thus genotypically modeling some late-stage human melanomas (*20*–*22*). The BRAF V600E variant has constitutively active kinase activity that up-regulates mitogen-activated protein kinase (MAPK) signaling and enhances aerobic glycolysis in cancer cells (*20*). Loss of PTEN enhances signaling through the PI3K/Akt/mTORC1 pathway, which also stimulates glucose metabolism (*23*–*25*). Cdkn2a silencing ultimately grants deregulated cell division and genetic instability through the deficit of p14 and p16 tumor suppressors, which cooperate with BRAF V600E in propagating tumorigenesis. Treating BRAF-mutant melanomas with BRAFi Mitogen-activated protein kinase kinase inhibitor (MEKi) shows an acute suppression of glucose metabolism (*26*, *27*). Therapy with dabrafenib (BRAFi) and trametinib (MEKi) has Food and Drug Administration approval, both as individual agents and in combination, to target this mechanism (*28*). Reduced tumor growth and glucose consumption has been observed in animals bearing Yumm1.7 flank tumors treated with BRAFi and MEKi compared to control animals (*26*, *29*). Previous studies on BRAFi and MEKi as well as other cancers have demonstrated treatment-induced perturbations in glycolysis by FDG-PET imaging and isotopomer analysis with [U-^{13}C]glucose, but none have assessed [$^2H_7$]glucose consumption and/or HDO production.

We demonstrate that imaging total deuterium (^2H) signal and spectroscopically measuring deuterated water (HDO) production from [$^2H_7$]glucose increases tumoral metabolic contrast and readily allows tumor detection and treatment monitoring. This result was achieved by the implementation of straightforward gradient echo imaging and 1D in vivo spectroscopy, both of which are simple MRI protocols that are readily available on clinical systems. In addition, to our knowledge, we are the first to image [$^2H_7$]glucose utilization to detect tumors and assess the efficacy of targeted therapies in vivo.

RESULTS

Established BRAFi and MEKi dose response by Western blot analysis

To assess the effectiveness of BRAFi and MEKi combinatorial treatment on signaling, we performed a dose response from low (0.1 μM BRAFi and 0.005 μM MEKi) to high (20 μM BRAFi and 1 μM MEKi) concentrations and performed Western blot analysis on control and treated Yumm1.7 cells in culture. We probed the blot with phosphorylated extracellular signal–regulated kinase (pERK) and ERK antibodies as they are downstream targets of BRAF and MEK. Figure S1 demonstrates reduced pERK and pERK/total ERK ratios at the low concentration with no ERK phosphorylation signal at the medium or high concentration (fig. S1, A to G).

BRAFi and MEKi therapeutic activity can be monitored with HDO production in vitro

On the basis of our findings, the medium concentrations of BRAFi (1.5 μM) and MEKi (0.07 μM) were selected for use in a cell culture [$^2H_7$]glucose tracer study. Specifically, these concentrations achieve maximal inhibition of MAPK signaling (fig. S1, A to F) with only a modest reduction in cell number (fig. S1G). Treatment induced alterations in signaling were matched by large changes in metabolites in the ^2H NMR spectrum (Fig. 1). Treatment significantly reduced the rates of extracellular glucose consumption, HDO production, and ^2H-lactate production by 64, 50, and 74%, respectively (Fig. 1, A to F). Intracellular concentrations of ^2H-lactate were significantly reduced by treatment and ^2H-glx concentrations were lower in treatment (fig. S1H). In addition, both ^2H-lactate and HDO were found to be highly correlated with [$^2H_7$]glucose consumption, with correlation coefficients (r) of 0.99 and 0.99, respectively (fig. S1, I and J).

Gas chromatography–mass spectrometry (GC-MS) analysis of control and treated cells revealed major central disruptions that contributed to reduced HDO and lactate production (Fig. 1, G to M).

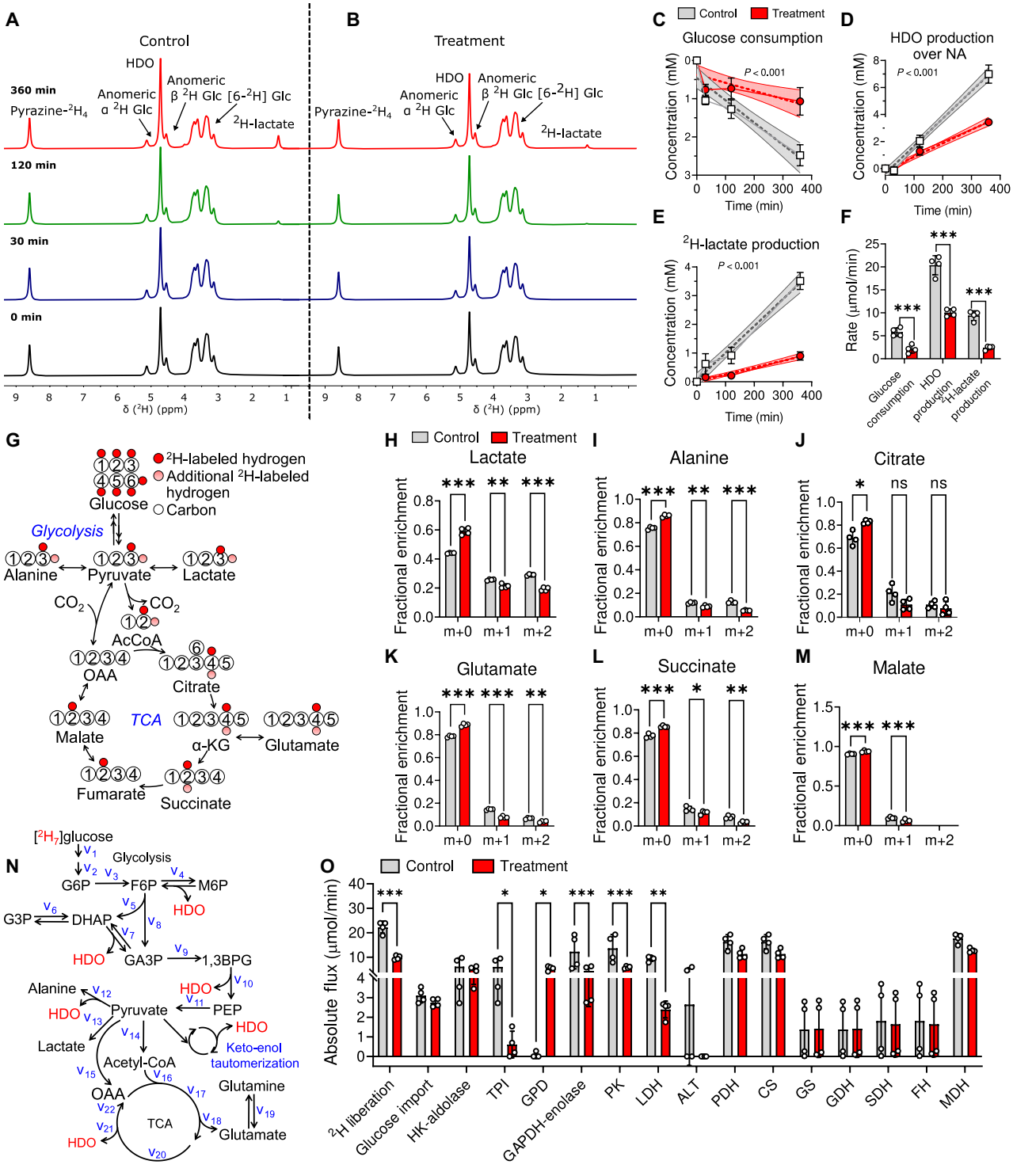

Fig. 1. In vitro characterization of the effects of treatment on glucose utilization. Combinatorial treatment leads to a significant downregulation of [$^2H_7$]glucose utilization detected by HDO production in cell culture. (**A** and **B**) Representative ^2H spectra of media samples collected across 6 hours from control and treatment groups, respectively. (**C** to **F**) Quantitative ^2H NMR kinetic data demonstrating that treatment reduces glucose consumption, HDO production over NA, and ^2H-lactate production in a sensitive manner. (**G**) Representative schematic of expected ^2H labeling patterns from [$^2H_7$]glucose utilization. (**H** to **M**) Fractional enrichments of major glycolytic and TCA cycle intermediates demonstrate a significant decrease in central carbon metabolism contributing to reduced HDO production. (**N**) Representative schematic of metabolic model designed to assess changes in flux. See Table 1 for a list of abbreviations. (**O**) Treatment decreased flux in pathways involved with HDO production. Linear regression analysis was used to establish significantly different kinetic slopes. Student's *t* test was used to establish significance between control and treatment rates of glucose utilization. Two-way analysis of variance (ANOVA) was used to establish significance across treatments, metabolite pool sizes, specific mass ion species, and flux measurements. Statistically significant changes are labeled as $*P \leq 0.05$, $**P \leq 0.01$, and $***P \leq 0.001$. Where not visible, SD error bars are behind symbols. ppm, parts per million.

Table 1. List of Abbreviations.

Fig. 1N Label	Abbreviation	Enzyme/Flux
v_2	HK	Hexokinase
v_6	GPD	Glycerol-3-Phosphate Dehydrogenase
v_7	TPI	Triosephosphate Isomerase
v_9	GAPDH	Glyceraldehyde-3-Phosphate Dehydrogenase
v_{11}	PK	Pyruvate Kinase
v_{12}	ALT	Alanine Aminotransferase
v_{13}	LDH	Lactate Dehydrogenase
v_{14}	PDH	Pyruvate Dehydrogenase
v_{15}	PC	Pyruvate Carboxylase
v_{16}	CS	Citrate Synthase
v_{18}	GDH	Glutamate Dehydrogenase
v_{19}	GS	Glutamine Synthase
v_{20}	SDH	Succinate Dehydrogenase
v_{21}	FH	Fumarate Hydratase
v_{22}	MDH	Malate Dehydrogenase

Decrements in fractional enrichment were matched by significant decreases in metabolite pool sizes with the exception of alanine, which increased significantly (fig. S2). Lactate-to-alanine ratios were significantly higher in control cells (~52) compared to treatment (~9) (fig. S3A). Fractional enrichments and kinetic rates from ^{2}H NMR measurements of glucose consumption, HDO production, and ^{2}H-lactate production were used as inputs to generate absolute flux measurements by using a [$^2H_7$]glucose utilization metabolic model written in the Isotopomer Network Compartmental Analysis (INCA) software (Fig. 1N and table S2). Analysis revealed treatment-induced decreases in glycolytic flux without substantially altering tricarboxylic acid (TCA) cycle turnover (Fig. 1O).

In addition, global metabolomics analysis with multivariate statistics demonstrated distinct differences in the metabolic profile of control and treated cells. Principal components analysis (PCA) showed clear separation between control and treatment groups with a PC1 of 76.9% (fig. S4A). Hierarchical heatmap clustering demonstrated excellent unsupervised clustering of control and treatment groups as well as corroborated significant decreases in glycolytic and TCA cycle metabolites caused by treatment (fig. S4B). Pathway enrichment analysis of the top 25 metabolites that were significantly different between control and treated cells revealed significant enrichment of several central pathways connected to HDO production (fig. S4C). Thus, extracts of cultured cells also demonstrate strong treatment-driven separation by PCA.

DMRI with [$^2H_7$]glucose can detect tumor metabolism in vivo

To test the in vivo applicability of this model, we injected Yumm1.7 cells into the right flanks of C57BL/6J mice, allowed for tumors to reach 10 to 15 mm, and imaged the animals before and after injection of [$^2H_7$]glucose. Our imaging protocol was established by optimizing a set of imaging and spectroscopy sequences that maximized the post-injection signal acquired. Axial slices allow for a comprehensive and simultaneous assessment of the tumor, contralateral healthy tissue, and phantoms of HDO and [$^2H_7$]glucose (Fig. 2, A and B). The optimization of imaging sequences culminated in an imaging workflow (Fig. 2C) that starts with animal setup, ^{1}H rapid acquisition with relaxation enhancement (RARE) contrasted anatomical images based on body water signal that allow the clear visualization of tumors as brighter signal, ^{2}H fast low angle shot (FLASH) gradient echo pre-injection images that acquire total ^{2}H signal and non-localized/localized spectroscopy that allows kinetic tracking of the production and consumption of metabolites, ^{2}H FLASH post-injection images and spectroscopy, and final ^{1}H images for anatomical referencing during quantitation. ^{2}H images were acquired with superior in-plane and interpolated resolutions of ~1 (1.09) and 0.27 mm^2 with an acquisition times of ~13 min for ^{2}H FLASH.

Image quantification used region of interest (ROI) mapping to reproducibly assess metabolic activity in all image overlays generated (Fig. 2D). The mean intensities measured within each ROI were used as inputs for total signal estimates described in detail in the methods. Quantification of the ^{2}H FLASH images acquired allowed for an average signal increase of ~2.3 within the tumor ROI, between post-injection and pre-injection images, indicating that our method can generate substantial metabolic contrast. Single-pulse spectroscopy (Fig. 2E) demonstrated a rapid increase in HDO signal post-injection of [$^2H_7$]glucose compared to pre-injection signal.

HDO imaging can be used to assess treatment efficacy in vivo

Yumm1.7 cells were injected into the right flanks of C57BL/6J mice, and once tumors reached ~10 mm in diameter, the mice were imaged to establish a baseline, and then control and treatment (BRAFi, 600 μg of dabrafenib; MEKi, 6 μg of trametinib) oral gavages were administered for 3 days followed by another round of imaging to assess the effects of treatment (Fig. 3A). Qualitatively, images showed notably reduced metabolic activity in treated tumors compared to control (Fig. 3, B and C). Image quantification showed significant reductions caused by treatment in tumoral measurements of ^{2}H signal. Treatment led to an 84% decrease in the total ^{2}H signal of tumors (Fig. 3D). Measurements of tumor mass and volume showed that treated tumors decreased in size and were significantly smaller than control tumors (Fig. 3E and fig. S5). Hematoxylin and eosin (H&E) histological analysis of paraformaldehyde-fixed and paraffin-embedded tumors demonstrated notably reduced cell density and greater evidence of necrosis in treated tumors compared to control (Fig. 3, F to I).

^{2}H spectra reveal tumor-specific decreases in metabolic activity caused by treatment

Throughout the imaging timeline, ^{2}H single-pulse (nonlocalized) and slice-localized spectroscopy were performed to track the kinetics of glucose utilization (Fig. 4 and fig. S6). Measurements of single-pulse spectra showed overall higher, but statistically insignificant, HDO production in baseline tumor bearing animals with no difference observed between control and treated animals (fig. S6A). Baseline, control, and treated tumor-bearing animals showed similar kinetics for glucose utilization (fig. S6B). Taking the ratio of HDO/glucose demonstrates a measurement of local HDO and [$^2H_7$]glucose. Single-pulse HDO/glucose ratios were not statistically different across all three groups but were slightly higher in control animals (fig. S6C). We used slice-localized spectroscopy, which allowed for the acquisition of spectra within selective slices placed separately on tumors and contralateral healthy tissues. The slices placed on tumors were set to minimize the inclusion of healthy tissue in the axial plane;

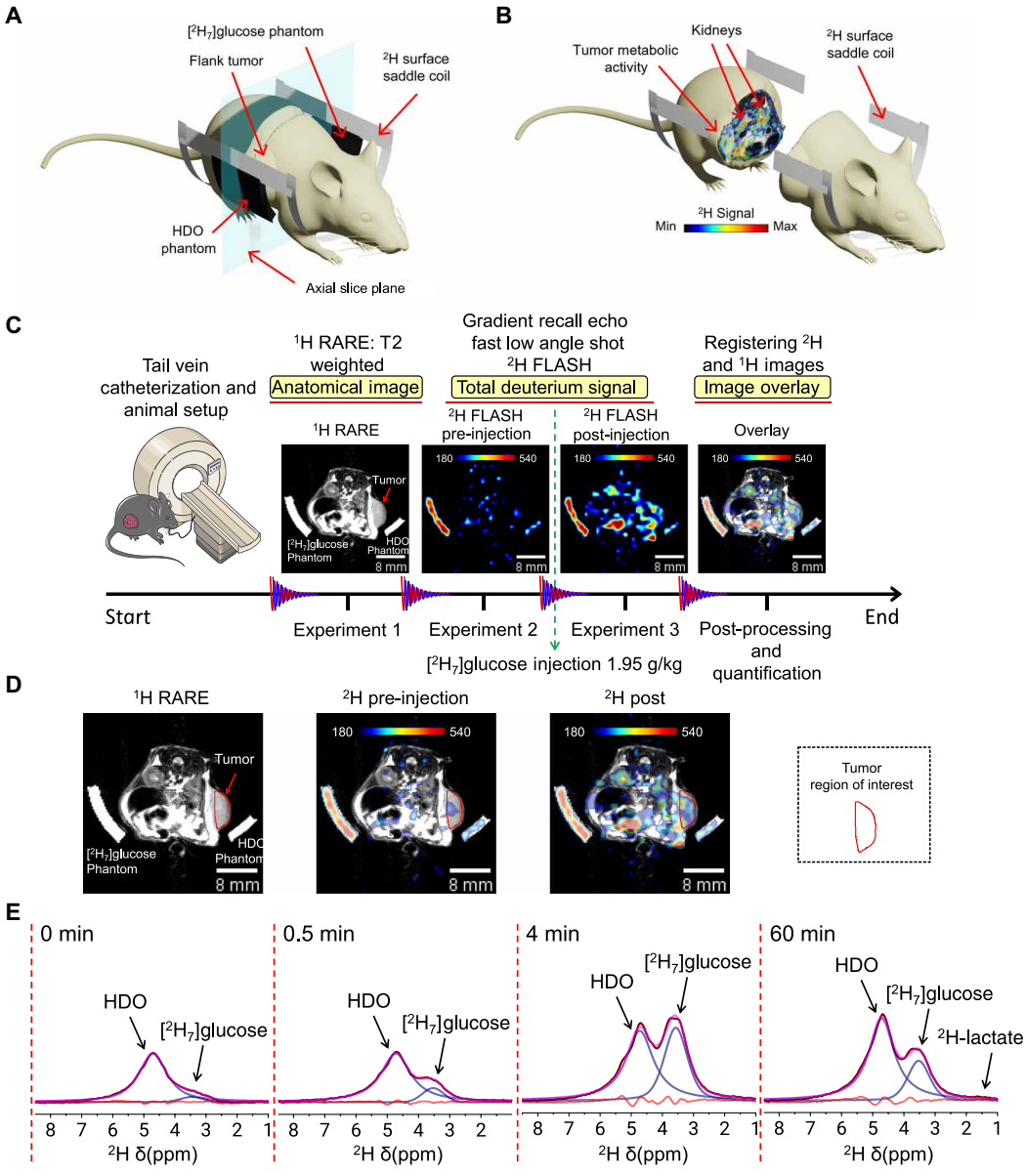

Fig. 2. Development of metabolically sensitive MRI for tumor detection. (**A** and **B**) Representative three-dimensional (3D) rendering of animal positioning and imaging slice selection with respect to the ^{2}H surface saddle coil and the anatomical positioning of the flank tumors. The ^{2}H image within the abdomen of the animal was acquired post-injection of [$^{2}H_{7}$]glucose, which generated signal primarily in the tumor and kidneys. (**C**) DMRI workflow established for the sensitive assessment of in vivo tumor metabolism. Workflow composed of a combination of ^{1}H anatomical images, ^{2}H pre-injection and post injection images, and ^{2}H spectroscopy throughout. (**D**) Region of interest (ROI) mapping-based image quantification allows for the analysis of tumor specific signal. (**E**) Representative nonlocalized ^{2}H spectroscopy time course of tumor bearing animal post-[$^{2}H_{7}$]glucose injection (1.95 g/kg). The small peak at 0 min arises from unsuppressed signal from the phantom.

however, some healthy tissue was unavoidable in the sagittal plane as the slice extends to max field of view (FOV) in this plane. The normalized signal intensities of slice selective spectroscopy showed that tumor tissue demonstrated faster initial kinetics than healthy tissue (Fig. 4A). No statistically significant differences were observed in localized glucose utilization, although overall greater glucose levels were observed in healthy control tissue (Fig. 4B). While not detected in single-pulse spectra, slice-localized spectroscopy allowed for the acquisition of ^{2}H-lactate signal in vivo. Control tumors generated the greatest amount of lactate compared to all other groups and tumors and, overall, were found to generate greater HDO/glucose ratios than healthy tissue (Fig. 4, C and D). Furthermore, at early time points control and treated tumors generated ~3× to 4× more HDO compared to contralateral healthy tissue. Given that some healthy tissue was covered by the slice-localized spectroscopy slice, all metabolites were normalized by tumor volume. Control tumors had up to ~6× more HDO as well as significantly greater glucose uptake/utilization and lactate production than treated tumors (Fig. 4, E to G). Although no statistical significance was established between control and treated HDO/glucose ratios from tumor volume–normalized measurements, control tumors trended to generate greater ratios (Fig. 4H).

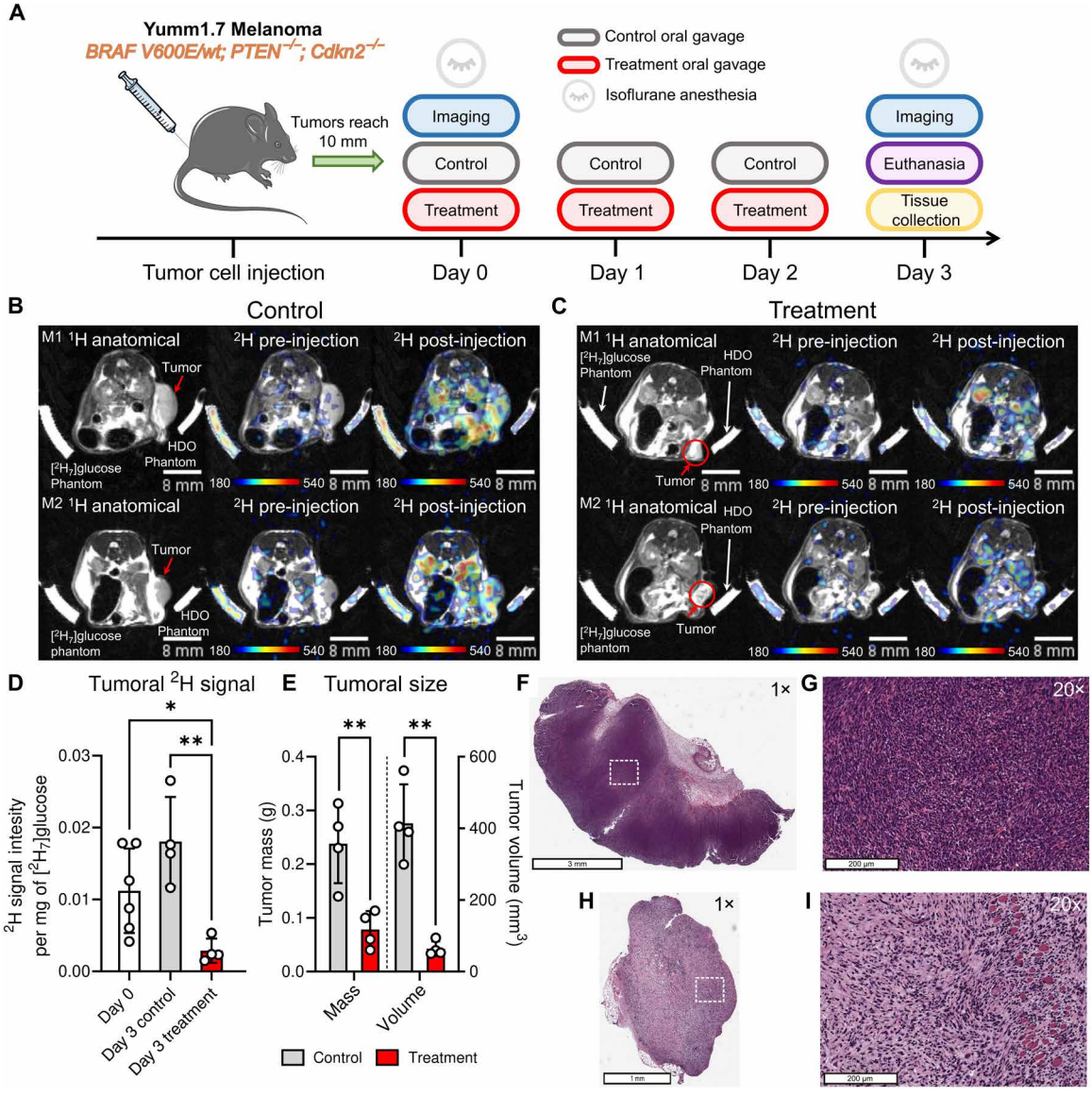

Fig. 3. Imaging [$^2H_7$]glucose utilization is sensitive to tumor metabolic activity. Total deuterium imaging (^{2}H FLASH) sensitively detects reductions in tumor metabolic activity. The overall experimental timeline is represented in (**A**). The images presented for all animals are as follows: ^{1}H RARE (T2-weighted anatomical image), ^{2}H pre-injection and post-injection (total deuterium image), and overlay (merged anatomical image with total deuterium image). (**B** and **C**) Images acquired for two control and two treated animals, respectively, before and after [$^2H_7$]glucose administration. (**D**) Quantitative data showing that imaging tumoral measurements of total ^{2}H signal are sensitive measures of therapeutic efficacy in vivo. (**E**) Tumor growth was assessed through the course of treatment and controls demonstrated significantly greater growth by final mass and volume. Representative H&E-stained control tumor at 1× (**F**) and 20× (**G**) and treated tumor at 1× (**H**) and 20× (**I**) shows reduced cell density and greater necrosis in treated tumors. The dashed box in 1× images highlights the area chosen for the 20× view for representative control and treated tumors. Student's *t* test was used to establish significance between baseline/day 0, control, and treatment animals. Statistically significant changes are labeled as $*P \leq 0.05$ and $**P \leq 0.01$.

[$^2H_7$]glucose DMRI is highly correlated with central metabolism

To assess the fate of [$^2H_7$]glucose derived ^{2}H, we assessed fractional enrichments, metabolite pool sizes, and metabolic flux through GC-MS analysis of tumors harvested after each imaging session. Similar to cell extract samples, tumoral measurements demonstrated significant treatment-induced decreases in m+1 and/or m+2 glycolytic and TCA cycle intermediates including lactate, alanine, glutamate, and succinate (Fig. 5, A to F). Pool size measurements showed significantly lower lactate in treated tumors and insignificant but modest decreases in glutamate and succinate (fig. S2B). Lactate-to-alanine ratios were significantly higher in control tumors (~39) compared to treatment (~30) (fig. S3B). INCA was used to generate a metabolic model (Fig. 1N and table S2) of tumoral flux that used metabolite fractional enrichments as inputs. Flux measurements were derived relative to glucose import to account for tracer uptake. Tumoral flux analysis revealed that treatment led to significantly reduced ^{2}H liberation, citrate synthase (CS), and malate dehydrogenases (MDHs) turnover

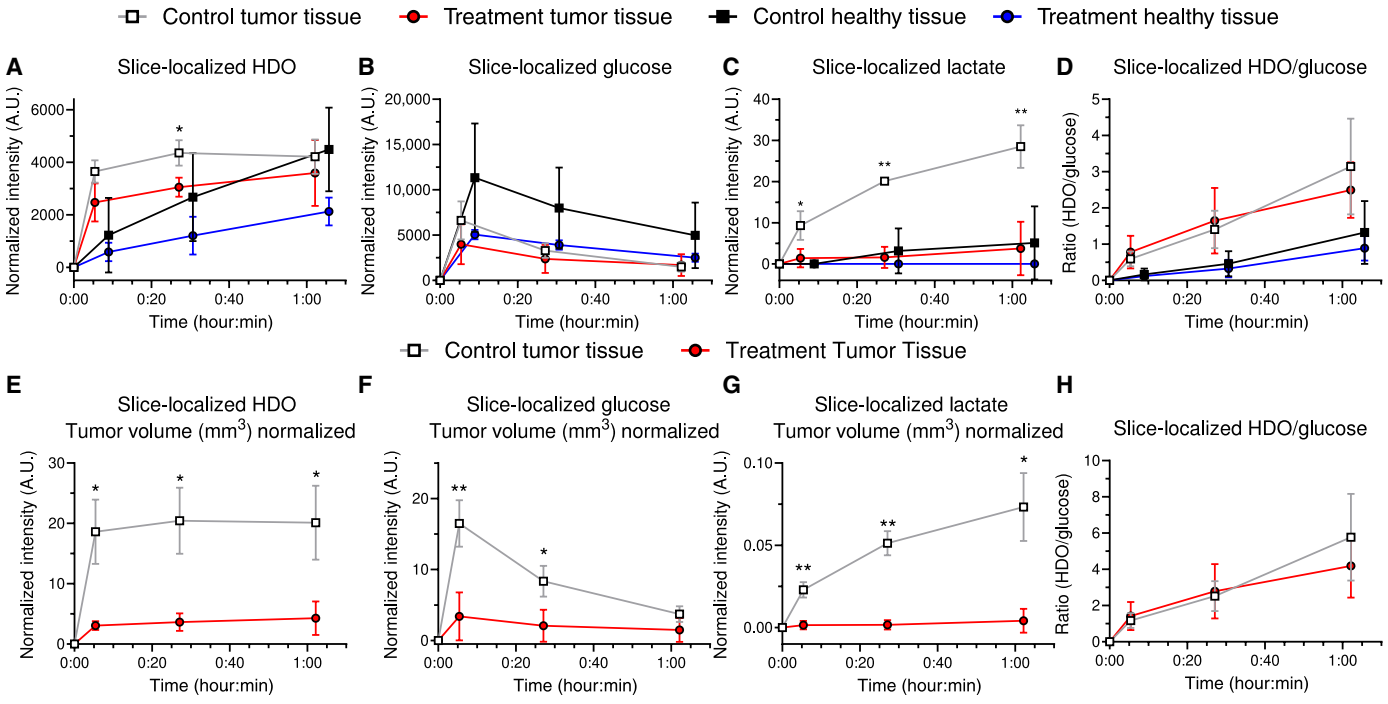

Fig. 4. ^{2}H spectroscopy reveals treatment-induced decreases in tumor metabolic activity. Slice-localized spectroscopy demonstrates distinct kinetic profiles between tumors and healthy tissue, and significantly higher metabolic activity in control tumors by measurements of HDO (**A**), [^{2}H$_7$]glucose (**B**), ^{2}H-lactate (**C**), and HDO/glucose ratios (**D**). (**E** to **H**) Tumor volume normalized data shows clear differences between the metabolic activity observed in control and treated tumors. Data are presented as the means ± SD of $N = 3$ biological replicates. Statistical significance was established by Student's t test and is labeled as $^*P \leq 0.05$, $^{**}P \leq 0.01$, and $^{***}P \leq 0.001$. Statistical marks are presented for differences between control and treatment tumors, other comparisons were not significant. A.U., arbitrary unit.

along with evident decreases in glycolytic reactions that contribute to HDO production through triosephosphate isomerase (TPI), glyceraldehyde-3-phosphate dehydrogenase (GAPDH)–enolase, and pyruvate kinase (PK) (Fig. 5G).

Total ^{2}H signal imaging (^{2}H FLASH) was demonstrated to be highly sensitive and correlated to treatment-induced reductions in tumor metabolic activity (Fig. 5, H to K). Measurements of total tumoral ^{2}H signal were positively correlated with lactate m+1 and succinate m+1 fractional enrichments, with r values of 0.81 and 0.81, respectively (Fig. 5, H and I). Stronger correlations were observed between tumoral HDO measurements and fractional enrichments (lactate m+1: $r = 0.89$ and succinate m+1: $r = 0.97$) (Fig. 5, J and K). In addition, these disruptions in central carbon metabolism were further supported by global metabolomics analysis of tumor extracts, which showed similar trends as the cultured cells, including treatment-induced reductions in glycolytic and TCA cycle intermediates and related pathways (fig. S4, D to F).

[^{2}H$_7$]glucose generates greater SNR and HDO than [6,6′-^{2}H$_2$]glucose

Given the strong readout of HDO production from [^{2}H$_7$]glucose utilization observed in vivo, we compared its performance to [6,6′-^{2}H$_2$]glucose by injecting equal doses of each tracer (1.95 g/kg) into different cohorts of tumor bearing mice and monitoring ^{2}H signal SNR and HDO production. Total ^{2}H signal images acquired with a ^{2}H gradient echo sequence demonstrates that [^{2}H$_7$]glucose can generate spatial maps of glucose utilization with greater signal and spatial resolution than [6,6′-^{2}H$_2$]glucose (Fig. 6A). Images acquired after [^{2}H$_7$]glucose injections showed distinct spatial localization resulting from organ-specific metabolism as observed by signal co-localized with kidneys, abdominal organs, and flank tumors. As a control of the spatial distribution of [^{2}H$_7$]glucose and a proxy of perfusion, we injected a third cohort of mice with 12.5% D_2O (5 μl/g body weight), a freely diffusible tracer. In contrast to [^{2}H$_7$]glucose images, total ^{2}H signal images acquired after D_2O injections showed no apparent spatial localization and signal appeared to be randomly distributed across the abdomen and tumor of the animals. ROI-based quantification of [^{2}H$_7$]glucose and [6,6′-^{2}H$_2$]glucose images allowed for an SNR analysis based on the mean signal intensity from a tumor region divided by the SD of the same noise region on the top left hand of all images. SNR calculations demonstrated that [^{2}H$_7$]glucose led to ~2× greater SNR compared to [6,6′-^{2}H$_2$]glucose (Fig. 6B). Slice-localized spectroscopy acquired throughout each imaging session showed that tumors administered with [^{2}H$_7$]glucose generated ~2.7× more HDO by 6 min post-injection than those administered with [6,6′-^{2}H$_2$]glucose (Fig. 6C). Nonlocalized single-pulse spectroscopy sampled some healthy tissue and tumoral metabolism, reporting significantly greater HDO production from [^{2}H$_7$]glucose than [6,6′-^{2}H$_2$]glucose (Fig. 6D).

DISCUSSION

Our findings demonstrate that DMRI with [^{2}H$_7$]glucose can be used as a metabolically sensitive paradigm for cancer detection and treatment monitoring in a safe and highly specific manner. We developed a

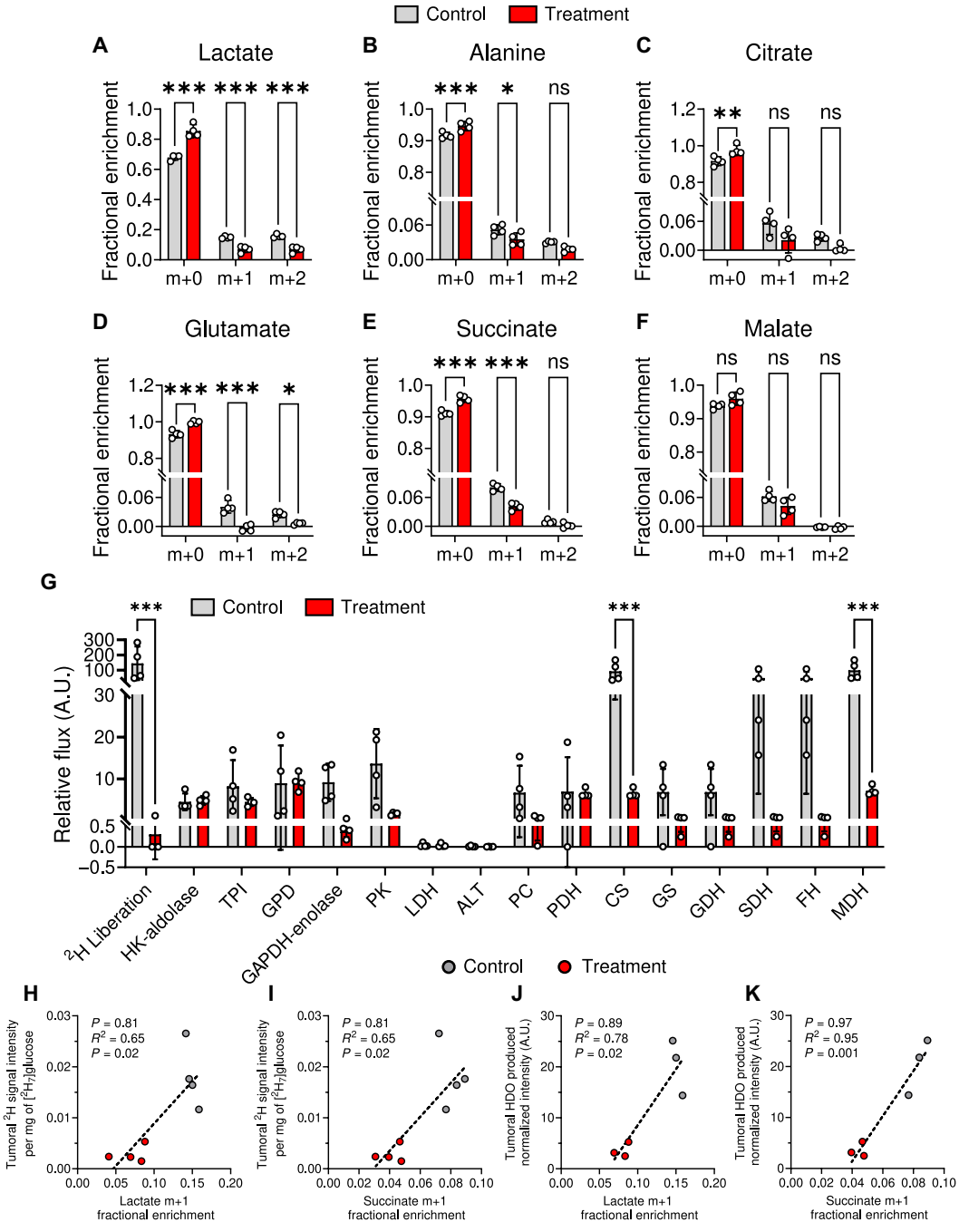

Fig. 5. Tumor treatments cause robust changes to central metabolism, correlating with overall observed HDO production. (**A** to **F**) Fractional enrichment analysis revealed treatment induced reductions in labeling of glycolytic and TCA cycle intermediates. (**G**) Metabolic flux analysis demonstrates extensive decrements in glycolytic and TCA cycle reactions involved in HDO production. (**H** to **K**) Tumoral ^{2}H signal and HDO measurements are strongly and positively correlated with lactate and succinate m+1 enrichments. These results demonstrate that the deuterium metabolic imaging treatment monitoring method presented is highly sensitive to tumor metabolic activity. Two-way ANOVA was used to establish significance across treatments, metabolite pool sizes, specific mass ion species, and flux measurements. Significant changes are labeled as $^*P \leq 0.05$, $^{**}P \leq 0.01$, and $^{***}P \leq 0.001$. Where not visible, SD error bars are behind symbols. Correlation analysis was performed to establish the statistical significance of the correlations.

robust imaging protocol and demonstrated its sensitivity to tumor metabolic activity by testing it with an established in vivo cancer model known to acutely perturb glycolysis. We acquired images of tumoral glucose utilization with metabolic contrast by imaging total ^{2}H signal and measuring HDO production after [$^2H_7$]glucose administration with straightforward, robust, and widely applicable methods. On the basis of our promising findings, we believe that this approach, using alternative deuterated tracers and measuring HDO production, can be used to assess and monitor a variety of diseases both before and during treatment.

To discern the key biochemical consequences of BRAFi and MEKi treatment on HDO production, we characterized the effects

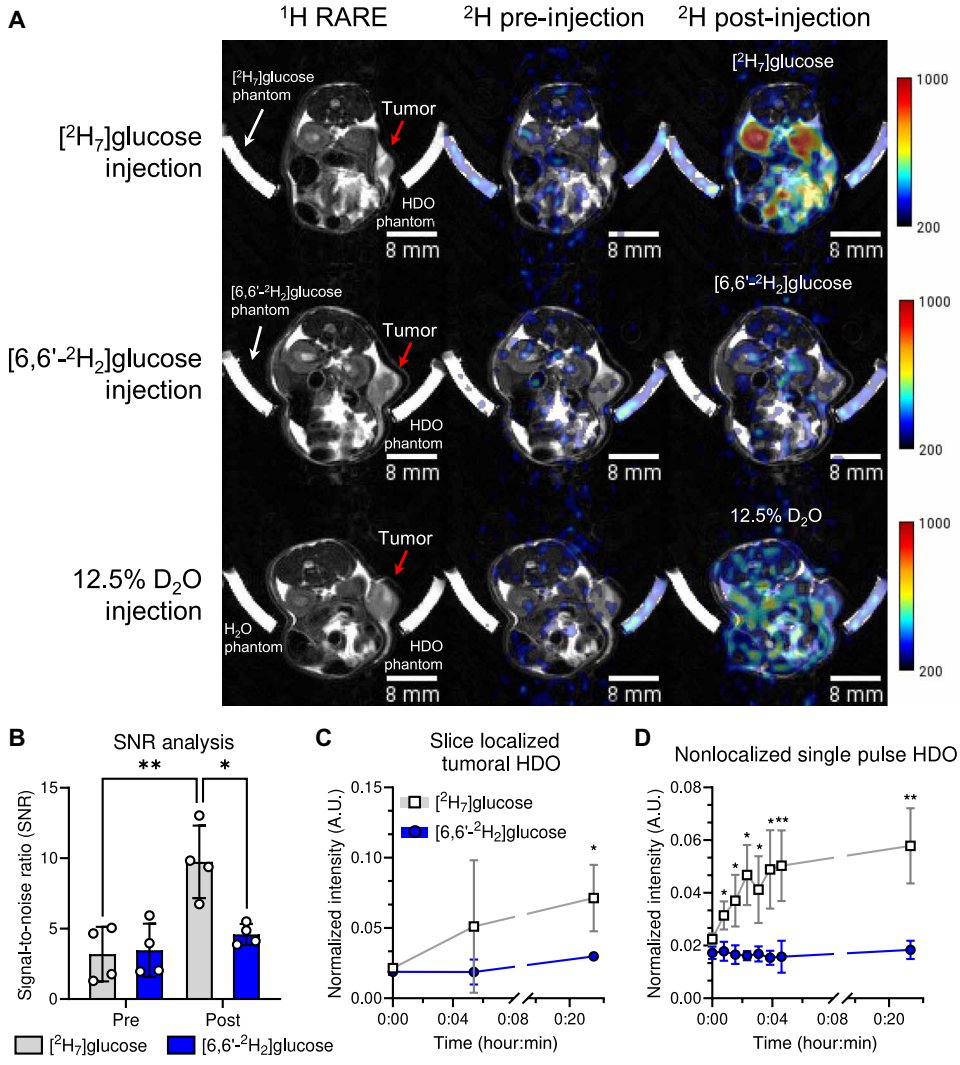

Fig. 6. HDO production from [$^2H_7$]glucose significantly improves SNR compared to [6,6′-$^2H_2$]glucose. (**A**) Three cohorts of animals were each injected either [$^2H_7$]glucose (1.95 g/kg), [6,6′-$^2H_2$]glucose (1.95 g/kg), or 12.5% D_2O saline (5 μl/g). Images for each injection are shown as follows: ^1H RARE images for anatomical referencing, pre-injection ^2H gradient echo images, and post-injection ^2H gradient echo images. (**B**) ROI-based quantification of tumoral signal mean intensity and noise standard deviation of [$^2H_7$]glucose ($N = 4$) and [6,6′-$^2H_2$]glucose ($N = 4$) images showed that [$^2H_7$]glucose led to significantly greater SNR. (**C**) Slice-localized ^2H spectroscopy demonstrated that tumors generated significantly greater HDO when using [$^2H_7$]glucose ($N = 4$) compared to [6,6′-$^2H_2$]glucose ($N = 3$). (**D**) Nonlocalized single-pulse spectroscopy also showed greater HDO production from [$^2H_7$]glucose ($N = 4$) compared to [6,6′-$^2H_2$]glucose ($N = 3$). All spectra here were quantified by dividing each peak by the pre-injection HDO peak area followed by a dose normalization. Student's *t* test was used to establish significance for SNR and spectroscopy data. Significant changes are labeled as $^*P \leq 0.05$ and $^{**}P \leq 0.01$. Where not visible, SD error bars are behind symbols.

of treatment on [$^2H_7$]glucose utilization in Yumm1.7 cells (Fig. 1 and fig. S1). We observed that HDO production was strongly correlated with [$^2H_7$]glucose consumption, indicating that HDO can serve as a reliable reporter of glucose utilization in vitro (fig. S1I). [$^2H_7$]glucose metabolism generates HDO through three-carbon glycolytic intermediate flux and through the utilization of deuterated acetyl-CoA (*18*). Given the fast rate of glycolytic metabolism and the relatively small intermediate pool sizes compared to the bolus of [$^2H_7$]glucose (*30*), ^2H spectroscopy allowed for the detection of glucose resonances with minimal contributions from intermediates. In addition, given the numerous reactions that contribute to HDO production, the final concentration of HDO detected in control cell culture was 8× higher than that of ^2H-lactate, highlighting the robustness of monitoring HDO production (Fig. 1, A to F).

^2H NMR data were further substantiated by GC-MS–based fractional enrichment analysis of Yumm1.7 cell extracts. As expected from previous reports, the overall enrichment of glycolytic and TCA cycle intermediates corroborates observed decreases in HDO production in a treatment-specific manner (Fig. 1, G to M). Note that unlike ^{13}C tracing, ^2H tracing is sensitive to label loss through processes such as isomerization, keto-enol tautomerization, and aminotransferase activity. For example, ^2H-lactate enrichment can be diluted by label loss through pyruvate keto-enol tautomerization and any pyruvate derived from ALT activity, which liberates a ^2H of the methyl group. Furthermore, pool sizes

matched treatment-specific decrements observed in metabolite labeling except for alanine, which was detected at higher levels in treated cells compared to control (fig. S2). Lactate-to-alanine ratios were significantly reduced by treatment, revealing a metabolic reversion to the state of healthy cells and away from Warburg metabolism (fig. S3). Absolute metabolic flux modeling based on cell fractional enrichments and glucose utilization rates revealed treatment-dependent decreases in reactions that directly contribute to HDO production including TPI, GAPDH to enolase, and ALT (Fig. 1, N and O). Reduced flux in TPI, LDH, and GPD is corroborated by literature on BRAF mutant melanomas. In addition to ERK/pERK, cMYC and hypoxia-inducible factor 1α (HIF1α) are also downstream targets of BRAF mutant hyperactivity. cMYC and HIF1α regulate lactate dehydrogenase (LDH) expression, and HIF1α regulates aldolase expression, controlling the substrate pool for TPI and GPD (*20*). Therefore, the reduction in MAPK signaling induced by BRAFi and MEKi treatment is predicted to reduce cMYC and HIF1α activity, culminating in reduced LDH, TPI, and GPD fluxes. The treatment-induced reduction of ALT flux (Fig. 1O) can account for decreased labeling and increased pool size, along with an increase in unlabeled alanine. Consistent with ^{2}H NMR data and fractional enrichments, flux analysis showed decrements in the major central metabolic steps of LDH, PDH, CS, and MDH, which together highlight decreases in glycolysis and TCA cycle activity that contribute to the observed decrease in HDO production (Fig. 1O).

Within the context of [U-^{13}C]glucose utilization, it has already been demonstrated that treating BRAF V600E mutant melanomas with BRAFi and MEKi leads to decreased glycolysis, contributing to decreased TCA cycle labeling (*20*, *26*). As shown in Fig. 1G, the utilization of [$^{2}H_7$]glucose can potentially liberate six deuterium labels as HDO molecules through glycolysis alone, with the final release of the remaining ^{2}H nuclei guaranteed through TCA cycle activity. Although nonlocalized single-pulse spectroscopy analysis showed trends of increased metabolic activity in control tumor bearing animals, these increases were not significantly different from treated animals (fig. S6). This is likely due to the nonspecific coverage of nonlocalized pulse-acquire spectra. Single-pulse spectroscopy acquires spectra for any tissues within the detection volume of the coil, thus these measurements account for tumor and healthy tissue metabolic activity. Overall, in vivo ^{2}H spectra generated similar line shapes to that of [6,6′-$^{2}H_2$]glucose. High-resolution spectroscopy can allow for the clear distinction of [$^{2}H_7$]glucose and [6,6′-$^{2}H_2$]glucose with the former having a complex superposition of peaks covering more parts per million (ppm) than the simple singlet of [6,6′-$^{2}H_2$]glucose. However, the line broadening effects observed in vivo merge the multiple peaks of [$^{2}H_7$]glucose into what appears to be a single peak similar to that of [6,6′-$^{2}H_2$]glucose.

Compared to ^{2}H-lactate detection from [6,6′-$^{2}H_2$]glucose, HDO production from [$^{2}H_7$]glucose has greater sensitivity because even before tracer is administered, the NA HDO provides a fairly good signal as a baseline. In the case of ^{2}H-lactate, a certain length of time must elapse before enough SNR is generated to observe the resonance. This becomes a limitation to early and fast kinetics as monitoring lactate would be challenged by the accumulation of sufficient signal for reliable MRI/S detection. Note most data published to date with [6,6′-$^{2}H_2$]glucose is acquired with oral administration of the glucose and then a waiting period before the imaging (*13*, *31*–*34*). This time delay is needed before lactate can be easily observed. From a metabolic standpoint, HDO is a more sensitive readout as it is produced at more steps, whereas [6,6′-$^{2}H_2$]glucose can only label half of glycolytically derived pyruvate (lactate), decreasing the overall sensitivity.

Our comparative in vivo analysis demonstrated that [$^{2}H_7$]glucose imaging generated ~2× more SNR than [6,6′-$^{2}H_2$]glucose imaging for equivalent weight of tracer administered (Fig. 6B). In addition, we show that ~2.7× more HDO can be produced from [$^{2}H_7$]glucose compared to [6,6′-$^{2}H_2$]glucose (Fig. 6C). The improved signal from [$^{2}H_7$]glucose fast imaging allowed for high metabolic contrast, which could not be achieved with [6,6′-$^{2}H_2$]glucose. The spatial localization and distribution of signal was completely different when an approximately equivalent dose of ^{2}H nuclei content as the [$^{2}H_7$]glucose injection (~2 M) was administered with 12.5% D_2O (~7 M) into tumor-bearing animals (Fig. 6A). Unlike the organ-specific localization of signal observed in [$^{2}H_7$]glucose images, D_2O images demonstrated nonlocalized signal randomly distributed across the abdominal organs, skeletal muscle, and tumors of the animals. This suggests that unlike the freely diffusible tracer, D_2O, [$^{2}H_7$]glucose is being used and handled by specific organs to different degrees. For example, images from [$^{2}H_7$]glucose injections showed negligible signal within the skeletal muscle surrounding the spine, which is likely due to the muscle relaxant effects of isoflurane anesthesia (Fig. 6A) (*35*). However, images after D_2O administration demonstrated signal within the skeletal muscle, thus highlighting the specificity of [$^{2}H_7$]glucose utilization (Fig. 6A). The presence of D_2O signal within the tumoral region indicates that tumors are perfused and that the signal generated after [$^{2}H_7$]glucose administration depends upon perfusion, uptake, and metabolism.

To isolate specific tissue types, we used slice-localized spectroscopy and found not only that tumors in control animals generated greater HDO than tumors in drug-treated animals but also that contralateral healthy tissue exposed to drug treatment had reduced metabolic activity compared to control healthy tissue (Fig. 4, A to D). These results suggest that treatment is affecting the metabolism of both tumors and healthy tissues, but with a greater effect in tumors. In addition, our method is sensitive to the metabolic differences between tumors and healthy tissue. Tumors had a distinct kinetic profile for HDO production that involved rapid initial HDO production that reached a maximum level at ~5.5 min and remained stable for 1 hour (Fig. 4A). In contrast, healthy tissue demonstrated linear kinetics throughout the course of the experiments with ~5.8× less HDO produced at early time points compared to tumors (Fig. 4A). This observation highlights the ability of our imaging methodology to distinguish tumors from healthy tissue with high specificity and sensitivity gained from rapid detection of high SNR HDO signal produced from [$^{2}H_7$]glucose.

The use of perdeuterated glucose maximizes total HDO production compared to other deuterated glucose analogs. In terms of financial cost, [$^{2}H_7$]glucose is ~2× to 3× more costly than doubly and singly deuterated analogs. There are two main approaches that can be taken to minimize the cost of deuterated glucose tracer. One is to continue to advance isotopic hydrogen-exchange techniques, which are more advantageous than approaches using biotechnology such as culturing algae in D_2O, which require biological expertise as well as extensive and complicated extraction processes (*36*). Another option would be to explore this methodology with [2,3,4,6,6′-$^{2}H_5$]glucose which has substrate costs estimated to be 10× less expensive than the deuteride substrates used for [6,6′-$^{2}H_2$]glucose and [$^{2}H_7$]

glucose synthesis (*37*). Given the high deuterium content of [$^2H_5$]glucose, it should generate similar SNR gains as [$^2H_7$]glucose while providing identical downstream labeling information.

Another consideration regarding the feasibility of [$^2H_7$]glucose clinical imaging is the ideal dose and mode of administration. The glucose doses used (1.95 g/kg) in this work were the same as the Yale studies performed by de Feyter *et al.* (*13*). However, other studies in humans have been able to generate metabolic contrast with doses as low as 0.75 to 0.8 g/kg (*31*, *38*). A dose-dependent imaging study will have to be performed to establish the ideal dose. Another aspect of administration is the mode, intravenous or oral. Oral glucose can lead to an incretin effect, which is a greater insulin response compared to intravenous administration. In addition, oral dosing requires more time for the tracer to be delivered throughout the body, which can somewhat limit the assessment of fast kinetics. Furthermore, the assessment of metabolism after oral administration of glucose can be complicated by contributions of the gut microbiota, which also consume the tracer. The gut microbiome is essentially bypassed by intravenous administration. Some of the next steps for clinical translation of this imaging exam would be to quantitatively assess the differences between oral and intravenous glucose administration and which kinetics would allow for the acquisition of maximal signal. Oral administration is the preferred method as it is straightforward and noninvasive; however, the delayed onset kinetics may miss early kinetic contrast generated by local HDO production. Once the administration avenue is established, several models of cancer and therapies will have to be assessed to build a reference of benchmarks for determining effective treatment by quantifiable reductions in HDO production.

The biochemical characteristics of [$^2H_7$]glucose utilization were leveraged to generate striking metabolic contrast in tumors by imaging in vivo tumor signal production with DMRI. We achieved requisite image acquisition with simple yet powerful gradient echo imaging sequences. These sequences allowed for high in-plane and interpolated resolutions of 1.09 and 0.27 mm^2, respectively. Total ^2H FLASH metabolic images allow for tumoral imaging assessing the effects of treatment with sensitivity to tumoral metabolic activity (Figs. 2 and 3). Tumoral HDO signal acquired by slice-localized spectroscopy had the strongest correlation with lactate and succinate m+1 enrichments compared to ^2H signal, thus highlighting the specificity of our method (Fig. 5). In corroboration, overall fractional enrichments, pool sizes, flux rates, and metabolic profile changes in tumor samples supported HDO production as a faithful reporter of tumor central metabolic activity (Fig. 5 and figs. S3 and S4). In the case of tumors, metabolic modeling was limited to deriving relative flux values, as opposed to absolute flux values, as another normalization paradigm such as estimates of O_2 consumption was not available. Unlike cultured cells, tumors displayed nonlinear kinetics in which HDO production rose to approximately max levels within 5 min and was maintained for 1 hour. To eliminate bias from the model, we chose to not use the in vivo tumoral kinetic rates as inputs for deriving absolute flux values. Instead, we derived relative flux values that agreed with all observations about the metabolic effects of treatment. However, these values contain some bias, as they were estimated, assuming an arbitrary 100% glucose import rate.

Moreover, this method is sensitive to treatment induced changes in metabolism. Analysis of pre-injection signal of day 0 and day 3 mice in ^2H FLASH images shows that our method can be performed serially with negligible pre-injection signal contribution 3 days post-[$^2H_7$]glucose administration that can be easily accounted for with pre-injection HDO normalization (fig. S7). The rapid rate of ^2H signal clearance post-[$^2H_7$]glucose administration may more readily allow the serial imaging of the same patient compared to methods that depend on the gradual incorporation of ^2H label over a multiple day period (*39*). With the acquisition of appropriate ^2H MRI coils for humans, ^2H FLASH sequences can be readily implemented into existing clinical MRI systems with minimal technical challenges as demonstrated by ^2H FLASH imaging for treatment monitoring at 1.5 T and numerous [6,6′-$^2H_2$]glucose studies performed at 3 T (*32*–*34*, *39*). The ^2H FLASH sequence used in this work implemented total scan times similar to clinical ^2H imaging at 3 T. The total scan time in this study for 256 averages was ~13 min. Each acquisition took ~3 s, but 256 averages were acquired to increase SNR. In comparison to 3 T, acquisition at 11 T allows for images with much higher resolution. Sequences were optimized to achieve maximal SNR; however when compared to 3 T, the higher resolution and the shorter T_2 would offset the benefits of a smaller coil and higher field. We have also noted through many experiments that increasing tissue mass exerts primary control over the SNR of experiments using isotopes to estimate metabolic flux. A whole human brain turns over a substantially higher amount of glucose (μmols/min) than a ~1 cm tumor in a mouse flank. In addition, the spectral quantification of 3 T data should be as straightforward as data acquired at high field because 11 T data presented here was unperturbed by the minor contributions of the α and β anomeric peaks.

In this initial iteration of treatment monitoring using the [$^2H_7$]glucose contrast agent, we chose to focus on developing our method in the most straightforward and reproducible manner. Therefore, we selected a flank tumor model as it allowed for simple implementation, easy detection of tumors, and ample residual tumor tissue for downstream analysis. To further document the robustness of this approach, future studies, can focus on an intrinsically derived orthotopic tumor model, as it may better model metabolic differences between tumors and adjacent non-malignant tissue as well as allow for testing the utility of this approach for the initial detection of tumors. Alternative tracers can also be explored, as HDO production from [$^2H_{15}$]octanoate has already been used as a quantitative imaging probe for dysregulated lipid metabolism (*40*), which is heavily implicated in cancer.

In addition, we can improve upon our imaging methodology by implementing chemical selectivity through fast chemical shift imaging (CSI). CSI is a well-known and regularly used MRI experiment but requires long acquisition times to acquire sufficient SNR. An alternative to this technique is already under way as efforts are being made to develop ^2H compressed-sensing CSI (CS-CSI) sequences that will allow for the fast acquisition of chemically sensitive images by under sampling image acquisition to achieve greater pixel averages and higher SNR. CSI-based approaches for ^2H imaging have already shown notable promise for generating chemically selective images with rapid acquisition (*41*–*44*).

We demonstrate the highly sensitive detection of differential glucose utilization across baseline, control, and treated tumors by measuring total ^2H signal and HDO production. Gradient echo imaging (^2H FLASH) generated total ^2H metabolic maps of colocalized HDO and [$^2H_7$]glucose, indicating that this method can be sensitive to perfusion/vascularity effects and metabolic effects. For example, at early time points (0 to 30 min), slices from the contralateral healthy tissue generated less HDO than tumor tissue, indicating that circulating

HDO generated from the [$^2H_7$]glucose agent is not driving the hyperintensity in the tumor. In addition, our in vitro modeling experiments, which are free of perfusion effects, show clear metabolic effects associated with treatment. In vitro, both control and treated cells were cultured with the same volume of media with equal concentrations of tracer. Cell extract analysis demonstrated reduced labeling in glycolytic and TCA cycle intermediates in treated cells. INCA modeling analysis accounted for reduced glucose import in treated cells and still demonstrated significantly reduced glycolytic flux in line with reduced HDO production. This suggests that even in the presence of perfusion effects, our model is still sensitive to metabolic effects. Nevertheless, future studies using this model should incorporate perfusion-based imaging to allow for the clear distinction of the perfusion/vascularity effects of a treatment (*45*).

Collectively, our findings show that HDO is a quantitative marker of tumor glucose utilization in vivo, and the imaging technique has translational potential in humans due to its safe classification, noninvasive oral administration, and suitability for routine treatment monitoring. Given the high in-plane (1.09 mm^2) and interpolated (0.27 mm^2) resolution achieved in this mouse study, the application of the current methodology to humans should lead to exemplary resolution without any substantial advancements in radio frequency coil technology, as this study used simple linear coil configurations. The development of human ^2H MRI coils for this technique is already underway and will allow for a future assessment of scalability of this approach in humans. In addition, the DMRI of HDO could lead to the development of more personalized treatment strategies mediated through serial imaging to inform a continuous reassessment regimen that establishes dosing based on the treatment response of the tumor. It is encouraging to note that imaging ^2H signal with a simple gradient echo sequence was highly sensitive in differentiating between the metabolic activity of control and treated tumors. This suggests that the methodology could provide a useful alternative to FDG-PET, with increased specificity from the detection of downstream metabolic products, without the use of ionizing radiation.

MATERIALS AND METHODS

Experimental design

We developed a robust imaging platform and tested the method by assessing therapeutic efficacy in a mouse flank tumor model. C57BL/6J mice were injected subcutaneously with highly glycolytic Yumm1.7 cells, which model late-stage human melanoma expressing constitutively active BRAF V600E protein. In vitro characterization demonstrated that treating Yumm1.7 cells with a combination of dabrafenib (BRAF inhibitor) and trametinib (MEK inhibitor) significantly reduced MAPK signaling as well as HDO production from [$^2H_7$]glucose. For in vivo treatment experiments, tumors were grown to ~10 mm in diameter, and mice were subsequently imaged to establish a baseline followed by oral gavage treatment with 600 μg of dabrafenib and 6 μg of trametinib for 3 days after which mice were imaged again to assess the effects of treatment. For imaging sessions, we intravenously injected with [$^2H_7$]glucose (1.95 g/kg) and imaged the mice on an 11.1 T scanner with a deuterium FLASH (^2H FLASH) sequence to acquire total ^2H signal. After experiments, cells and tumors were harvested and analyzed by GC-MS to establish pool sizes, fractional enrichment, and metabolic models for flux measurements.

Cell lines and cell culture reagents

Yumm1.7 cells were provided by the Children's Medical Center Research Institute at the University of Texas Southwestern Medical Center. Glucose-free Dulbecco's modified Eagle's medium/Ham's F-12 nutrient mixture (DMEM/F-12) was purchased from US Biological (Salem, MA, USA). Glucose-free medium was used to administer the glucose tracer to cells. For regular cell maintenance, 25 mM unlabeled D-glucose was supplemented. Deuterated pyrazine ([$^2H_4$]pyrazine), and D-glucose were purchased from Sigma-Aldrich, (St. Louis, MO, USA). [1,2,3,4,5,6,6-$^2H_7$]-D-glucose ([$^2H_7$]glucose) was purchased from Cambridge Isotope Laboratories (Andover, MA, USA). Fetal bovine serum (FBS) was purchased from Atlas Biological (Fort Collins, CO, USA). Phosphate-buffered saline (PBS), penicillin/streptomycin (P/S), nonessential amino acids (NEAAs), and dimethyl sulfoxide (DMSO) were purchased from Thermo Fisher Scientific (Waltham, MA, USA). Dabrafenib and trametinib were purchased from Selleck Chemical (Houston, TX, USA). Isoflurane anesthesia was obtained from Patterson Veterinary (Ocala, FL, USA). A 0.9% sterile filtered saline was prepared from NaCl purchased from Thermo Fisher Scientific (Waltham, MA, USA) and constituted with 5% sterile heparin (50 USP/ml, final concentration), to prevent clotting. Heparinized saline was used to dissolve the [$^2H_7$]glucose solution before administration to the animals. All reagents were sterile-filtered before administration to cells or animals.

Cell culture dose response and Western blot analysis

Yumm1.7 cells were treated with a dosing curve of combinatorial treatment (dabrafenib BRAFi and trametinib MEKi) ranging from low to high concentrations. The respective concentrations of BRAFi and MEKi utilized were 0.1 and 0.005 μM for low, 1.5 and 0.07 μM for medium, and 20 and 1 μM for high. After treating the cells for 24 hours, the cells were probed for pERK and ERK protein expression by Western blot analysis. Cells were harvested and immediately lysed with ice-cold radioimmunoprecipitation assay buffer supplemented with halt protease and phosphatase inhibitors (Thermo Fisher Scientific, Waltham, MA, USA). Protein concentrations were then established by a Bradford assay (Bio-Rad, Hercules, CA, USA) for normalization before gel loading. Protein-normalized cell lysates were loaded in a 4 to 20% Criterion TGX gel (Bio-Rad, Hercules, CA, USA), and proteins were separated by applying a constant 0.05 A to the gel. After the elution of the loading dye front, the gel was immediately transferred to a polyvinylidene fluoride membrane (Bio-Rad, Hercules, CA, USA) at a constant 50 V at 4°C for 1 hour. The membrane was then stained with fast green (Sigma-Aldrich, St. Louis, MO, USA) to ensure even protein loading. Then, the membrane was destained, washed, and blocked with 5% nonfat dry milk dissolved in TBS-T [200 mM sodium chloride (NaCl), 30 mM Tris-hydrochloric acid (HCl) (pH 7.6), and 0.1% Tween 20] for 1 hour. Proteins were probed with primary pERK (mouse monoclonal, Santa Cruz Biotechnology, Dallas, TX, USA), ERK (rabbit polyclonal, Santa Cruz Biotechnology, Dallas, TX, USA), and α-tubulin (mouse monoclonal, Cell Signaling Technology, Danvers, MA, USA) antibodies. Primary antibodies were diluted [pERK, 1:200 (v/v); ERK, 1:500 (v/v); and α-tubulin, 1:5000 (v/v)] with 5% nonfat dry milk dissolved in TBS-T and independently incubated with the blot for 18 hours at 4°C. After incubation with each primary antibody, the membrane blot was thoroughly washed and incubated with either

secondary anti-mouse horseradish peroxidase (HRP) antibody [1:5000 (v/v)] or secondary anti-rabbit HRP antibody [1:10,000 (v/v)] at room temperature for 1 hour. Once probed for secondary antibody, the blot was washed and reacted with PierceTM ECL Western Blotting Substrate (Thermo Fisher Scientific, Waltham, MA, USA) and then exposed to PRIMA1 autoradiography film (Midwest Scientific, Valley Park, MO, USA). Protein expression was quantified by densitometry analysis on ImageJ (National Institutes of Health, Bethesda, MD, USA).

Cell culture treatment and [$^2H_7$]glucose tracer administration

Yumm1.7 cells were maintained with complete growth medium composed of DMEM/F-12 with 10% (v/v) FBS, 1% P/S, and 1% NEAA. Cell lines were maintained at 37°C with 95% air and 5% total CO_2 in an air-jacketed incubator (Heracell Vios 160i, Thermo Fisher Scientific, Waltham, MA, USA). Every 2 to 3 days, complete medium was replaced, and once at 60% confluence, cells were subcultured 1:6 into eight 100-mm cell culture dishes. All cell lines were grown to 60% confluency and washed once with warm PBS and incubated with 10 ml each of either DMEM/F-12 with 1.5 μM BRAFi and 0.07 μM MEKi or DMEM/F-12 with a DMSO vehicle for 18 hours. After the 18-hour time point, all DMEM/F-12 was aspirated, cells were washed once with warm PBS and then incubated with 5-ml each of DMEM/F-12 containing the same concentrations of BRAFi and MEKi along with 11 mM [$^2H_7$]glucose for 6 hours, withdrawing 200 μl of aliquots at 0 min, 30 min, 2 hours, and 6 hours. Immediately after the 6-hour time point, cells were washed, trypsinized, and harvested for subsequent ^2H NMR and GC-MS analysis.

^2H NMR sample preparation

All media samples were processed and prepared without extraction. Each media sample was spiked with [$^2H_4$]pyrazine internal standard to a nominal concentration of 2.5 mM. The [$^2H_4$]internal standard allowed for the quantitation of HDO, ^2H-lactate, and residual [$^2H_7$]glucose from ^2H NMR data. A total of 180 μl of cell media sample for each time point was loaded into 3-mm NMR sample tubes for NMR analysis. Cells were extracted with acetonitrile:isopropanol:water [3:3:2 (v/v/v)], dried down, and further refined with acetonitrile:water [1:1 (v/v)]. Dried extracts were then reconstituted in water and transferred to 3-mm NMR tubes for NMR analysis.

^2H NMR analysis

A Bruker Bio-Spin 18.8 T magnet system equipped with an Avance III Console and 5-mm TXI CryoProbe and TopSpin 4.0.3 was used for ^2H NMR data acquisition of [$^2H_7$]glucose, HDO, ^2H-lactate, and ^2H-glx in the cell and media samples. The deuterium lock channel was used for ^2H NMR spectra acquisition at 122.79-MHz resonant frequency. An acquisition time of 2 s and a relaxation delay of 1 s (total, 3 s of repetition time) with a 90° pulse were used for acquisition. The 8190 complex data points were digitized with an 11-ppm spectral width and 256 scans for each of the three free induction decays (FIDs) (768 scans) for all samples. Data acquisition took place at room temperature (25°C).

After acquisition, ^2H NMR spectra were further processed with MestReNova v14.0.1-23284 (Mestrelab Research SL). ^2H NMR spectra were processed by setting the exponential window function to 0.5 Hz and increasing the zero filling of the FID to 16,384 data points performing fourier transformation. Automatic phase and spline baseline corrections were performed for each spectrum. All ^2H NMR spectra acquired for each sample were aligned with respect to the [$^2H_4$]pyrazine peak and summed to account for peak shifting caused by magnetic field drift during experimental acquisition. Concentrations of ^2H-labeled metabolites in cell and media samples were calculated using the internal standard peak area of [$^2H_4$]pyrazine. The known concentration of [$^2H_4$]pyrazine (2.5 mM) was leveraged for the quantification of HDO and residual [$^2H_7$]glucose concentrations, which were normalized to the total number of deuterium nuclei responsible for the respective peak resonances.

GC-MS sample handling and analysis

GC-MS sample preparation (cell, media, and tumor samples), instrument analysis, data processing, and metabolomics statistical analysis were performed exactly as previously published (*19*, *46*–*49*). Metabolomic profiling was based on the metabolite panel presented in table S1. The Thermo Scientific Single Quadrupole Mass Spectrometer (ISQ) and Gas Chromatograph (TRACE 1310) were used for all analyses.

Fractional enrichment and metabolic modeling analysis

Mass isotopomer distributions (MIDs) were generated by integrating the extracted ion chromatograms of each metabolite identified by GC-MS using QuanBrowser on XCalibur 4.5 (Thermo Fisher Scientific, Waltham, MA, USA). Metabolite MIDs were further processed by NA correction using the INCA software (INCA 2.0, Vanderbilt University, Nashville, TN, USA) (*50*, *51*). INCA was also used to develop a mathematical metabolic flux model of [$^2H_7$]glucose utilization to estimate the absolute and relative flux measurements of pathway contributions to HDO production. These reactions are detailed in table S2. The model was constructed to mimic the metabolic processes of glucose import, glycolysis, TCA cycle, and key components of shuttle systems such as the malate-aspartate shuttle and citrate-malate mitochondrial carrier. In addition, it accounted for sources of acetyl-CoA such as fatty acid oxidation. Specific steps generating reduced form of nicotinamide adenine dinucleotide or $FADH_2$ were included, followed by the assumed consumption of O_2 through oxidative phosphorylation. Metabolic intermediates not identified through GC-MS analysis were omitted from the model, for instance, flux from citrate to α-ketoglutarate was simplified as a single step. Metabolite fractional enrichments were calculated by inputting the mass isotopomer distribution of specific metabolites from mitochondrial experiments and their chemical formulas into INCA's NA correction function, as previously described.

In vivo flank tumor imaging model

All experimental procedures on animals were approved by the University of Florida Institutional Animal Care and Use Committee under protocol 202400000077. Male C57BL/6J mice were purchased from the Jackson Laboratories and acclimated in the animal housing facility. For in vivo experiments, tumors were grown to ~10 mm in diameter, and mice were subsequently imaged to establish a baseline followed by oral gavage treatment with 600 μg of dabrafenib and 6 μg of trametinib for 3 days after which mice were imaged again to assess the effects of treatment. During treatment, tumor volume was monitored by ^1H MRI (days 0 and 3) and caliper measurements (days 1 and 2). Caliper data were quantified by calculating the volume approximations ($V = 0.5 \times l \times w^2$) of the tumors. For imaging sessions, animals were anesthetized with 5% isoflurane and maintained under

anesthesia until the end of the session. Animals were tail vein catheterized and hydrated with 0.9% saline containing 5% heparin. Animal body temperature was maintained at 37°C with heated circulating water lines, and respiration was monitored with a respirometer for the entire extent of the imaging session. Once shimming and pre-injection images were acquired, the animals were injected with [$^2H_7$] glucose (1.95 g/kg) for at a rate of 50 μl/min (~2 min). ^{1}H anatomical MRI images were used to determine tumor volume measurements by calculating the approximate hemi-ellipsoid volumes of tumors ($V = \pi/6 \times a \times b \times c$). At the end of imaging sessions, animals were humanely euthanized, and tumors were extracted, weighed, and stored for subsequent analysis. We present estimates of tumor volume using caliper measurements of days without the MR imaging portion of the paradigm and the more accurate ^{1}H MRI to produce the correlations with the metabolic imaging data. While these two estimates varied slightly in scale, the relative changes between control and treatment tumors matched the expected changes in growth through the course of therapy.

Another subset of animals was used to test a comparison between [$^2H_7$]glucose, [6,6′-$^2H_2$]glucose, and D_2O injections. The imaging protocol was followed exactly as detailed above including dosage which was kept at 1.95 g/kg for both glucose tracers. Similarly, D_2O experiments followed the same protocol, but imaging sessions were concluded immediately after the ^{2}H FLASH image. D_2O injections (12.5%) were administered with 0.9% heparinized saline at a dose of 5 μl/g. All animals in this subset were imaged with a 9-mm slice. Phantoms were used as follows: 10 mM deuterated glucose, 0.125% D_2O, and plain water used as the left phantom for D_2O imaging.

MRI scanner and hardware

All animal imaging sessions were performed on an 11.1 T Magnex magnet integrated with a Bruker Avance III HD console controlled by ParaVision 6.0.1 (Bruker Biospin, Billerica, MA). The MRI scanner was outfitted with a RRI BFG-240/120-S6 gradient coil (120 mm in bore size), which is capable of generating 100 mT/m with a 200-μs slew rate. A B0 map was acquired for localized shimming on the animal abdomen by using an 85-mm home-built, actively decoupled, linear volume ^{1}H transmit-receive coil operating at 470 MHz. For deuterium spectra and image acquisition, a home-built 26-mm diameter, ^{2}H half-saddle coil tuned to 72.26 MHz was used. The ^{2}H half-saddle coil was placed within a custom three-dimensional (3D) printed animal cradle suitable for abdominal imaging. Animals were placed into the cradle such that the abdomen and tumor region were within the midline and isocenter of the coil. Two phantoms were 3D printed and independently filled with 20 mM [$^2H_7$]glucose and 0.125% (v/v) D_2O. Both phantoms were superficially attached to the exterior of the half-saddle coil and used to confirm positioning and quality control for image and spectroscopy quantification.

Deuterium metabolic imaging

Axial ^{1}H images of the abdominal cross section covering the tumor region of mice were acquired using a FLASH gradient echo sequence and/or a RARE spin-echo sequence. A 2D acquisition matrix size of 128 × 128 and FOV of 35 mm by 35 mm were used to acquire 10 to 14 slices (2-mm slice thickness) of mice abdomen. Before the [$^2H_7$]glucose injection, a pre-injection ^{2}H image capturing total ^{2}H signal of the mouse abdomen region covering the tumor was acquired using a ^{2}H FLASH sequence, with the ^{2}H water (HDO) signal set on resonance. At approximately 10 min post-injection, another ^{2}H FLASH image was acquired. The following parameters were used for the acquisition of axial ^{2}H images of the mouse abdomen: matrix size = 32 × 32, FOV = 35 mm by 35 mm, slice thickness = 4 to 10 mm (set specifically to only cover the tumor region), TR = 100 ms, 256 signal averages, 1.416-ms time-to-echo (TE), and 30° flip angle. The acquisition of each ^{2}H FLASH image took ~13 min.

Deuterium MRI

Before experiments, the performance of the ^{2}H coil was verified by calibrating and optimizing the radiofrequency pulse and flip angle to ensure maximum ^{2}H signal acquisition. The NA of deuterium (0.015%) accounts for ~17 mM naturally derived HDO that appears as a single peak in ^{2}H spectra. To account for system and biological variations within each animal imaging session, the HDO signal detected in pre-injection single-pulse acquire spectra was used to normalize all spectra post-[$^2H_7$]glucose injection. The acquisition was achieved with a spectral width of 4 kHz, 1024 data points, a 300-ms time-to-repeat (TR), a 60° flip angle, and 512 scans. Each single-pulse acquire experiment lasted a total 1.28 min. Spectra were acquired throughout the course of the imaging session. To gain tissue selectivity, we also used slice-localized spectroscopy to acquire data from sagittal slices (perpendicular to axial images) placed on tumor and separately on contralateral healthy tissue. Spectral acquisition was accomplished with a 3-kHz spectral width, 512 data points, a TR of 100 ms, a flip angle of 60°, and 2048 averages. Slice thickness varied based on tumor size but remained within 3.5 to 5.5 mm across all animals. The total acquisition time for each experiment was 3.34 min. All ^{2}H spectra were processed using MestReNova v14.0.1-23284 (Mestrelab Research SL). Line broadening was set to 10 Hz, spectra were zero filled to twice the number of data points, and spectra were baseline corrected with the Whittaker smoother function. All spectra were line-fitted and deconvolved to extract peak areas, which were used to quantitate the normalized intensities of HDO, [$^2H_7$]glucose, and ^{2}H-lactate. Single-pulse spectra were quantified by normalizing each peak area (HDO, [$^2H_7$]glucose, and ^{2}H-lactate) by the pre-injection HDO peak area. This value was then divided by the dose of [$^2H_7$]glucose (milligram) administered (Eq. 1). The areas of slice-localized spectra obtained after administration of [$^2H_7$]glucose were corrected for naturally present HDO by subtracting pre-injection values from post-injection values. These values were then divided by the amount (milligram) of [$^2H_7$]glucose administered (Eq. 2). [$^2H_7$]glucose and ^{2}H-lactate peak areas were directly normalized by the amount (milligram) of [$^2H_7$]glucose dosed (Eq. 3). This first quantification of slice-localized spectroscopy allowed for a comparison of tumor and healthy tissues. To account for tumor volume and a more direct comparison between control and treated tumors, slice-localized spectra were quantified by a second process. In this quantification, the pre-injection HDO peak area was normalized to tumor volume (cubic millimeter) to account for the amount of tumor tissue analyzed per animal since it contributes to the amount of pre-injection HDO detected. The mean intensity of the tumor was divided by the normalized pre-injection HDO peak area. This value was then dose normalized to account for the amount (milligram) of [$^2H_7$]glucose administered per animal (Eq. 4)

$$\text{Normalized Peak Area (A. U.)} = \frac{\text{Peak area of metabolite of interest (A. U.)} / \text{Pre-injection HDO peak area (A. U.)}}{\text{Dose of } [^2H_7]\text{glucose (mg)}} \quad (1)$$

$$\text{Normalized Peak Area (A. U.)} = \frac{\text{HDO post-injection peak area} - \text{HDO pre-injection peak area}}{\text{Dose of } [^2H_7]\text{glucose (mg)}} \quad (2)$$

$$\text{Normalized Peak Area (A. U.)} = \frac{[^2H_7]\text{glucose or } ^2\text{H-lactate post-injection peak area (A. U.)}}{\text{Dose of } [^2H_7]\text{glucose (mg)}} \quad (3)$$

$$\text{Normalized Peak Area (A. U.)} = \frac{[\text{Peak area of metabolite of interest (A. U.)}] / \left[\frac{\text{HDO pre-injection peak area (A.U.)}}{\text{Tumor volume } (mm^3)}\right]}{\text{Dose of } [^2H_7]\text{glucose (mg)}} \quad (4)$$

Image processing

All image processing was performed with ImageJ (National Institutes of Health, Bethesda, MD, USA). To coregister and overlay ^{1}H and ^{2}H images, all ^{2}H images (acquired with a 32 × 32 matrix size) were interpolated with bicubic processing to a 128 × 128 image size to match the size of ^{1}H images. Signal quantitation involved gathering the mean signal intensity within the tumor tissue region and the peak area of the pre-injection HDO peak of slice-localized spectroscopy covering tumor tissue. The pre-injection HDO peak area was normalized to tumor volume (mm^3) to account for the baseline amount of HDO present in tumor tissue. The mean intensities of tumor ROIs in ^{2}H FLASH images were divided by the normalized pre-injection HDO peak area. This value was then dose normalized to account for the amount (mg) of [$^2H_7$]glucose administered per animal. Slice-localized spectroscopy was setup to sample the maximal tumor volume while minimizing contributions from the healthy tissue. The HDO peak area of slice-localized spectroscopy was chosen instead of the mean intensity of the pre-injection tumor ROI because the HDO peak in ^{2}H spectra had over 10× more SNR than the tumoral mean intensities across animals. For the [$^2H_7$]glucose and [6,6′-$^2H_2$]glucose comparative study, image SNR calculations were performed by dividing the mean intensity of each tumor ROI by the SD of the same noise ROI placed on the top left-hand corner of all images. The data processed for SNR calculations was magnitude data; therefore, a correction factor (square root of 2-π/2) was applied to the SD of noise to account for the Rician distribution of noise (*52*).

Histology

Upon harvesting, approximately half of each tumor was immediately placed into a histology cassette and subsequently in a solution of 4% (w/v) paraformaldehyde in PBS. The tumors were incubated in this solution for ~18 hours. At the end of this time, the tumor samples were transferred to 70% ethanol for another 24 hours and then transferred to fresh 70% ethanol for a final 24 hours. The samples were maintained in 70% ethanol at 4°C until they were submitted to the UF Molecular Pathology Core for further processing. The fixed tumor tissues were paraffin embedded, sliced, stained with H&E, and imaged.

Statistical analysis

The specific statistical analysis performed for each dataset is reported under each figure. Grouped datasets were analyzed by one-way or two-way analysis of variance (ANOVA) with Tukey post hoc multiple correction. Column datasets were analyzed by Student's *t* test. Correlations were analyzed by correlation matrix analysis. A *P* value of 0.05 or lower was considered significant. All statistics were performed and analyzed with GraphPad Prism 9 (version 9.5.0).

Supplementary Materials

This PDF file includes:

Figs. S1 to S7

Tables S1 and S2

REFERENCES AND NOTES

1. R. L. Siegel, A. N. Giaquinto, A. Jemal, Cancer statistics, 2024. *CA Cancer J. Clin.* **74**, 12–49 (2024).
2. J. D. Schiffman, P. G. Fisher, P. Gibbs, Early detection of cancer: Past, present, and future. *Am. Soc. Clin. Oncol. Educ. Book* **2015**, 57–65 (2015).
3. J. T. Loud, J. Murphy, Cancer screening and early detection in the 21st century. *Semin. Oncol. Nurs.* **33**, 121–128 (2017).
4. L. Fass, Imaging and cancer: A review. *Mol. Oncol.* **2**, 115–152 (2008).
5. N. K. Tafreshi, V. Kumar, D. L. Morse, R. A. Gatenby, Molecular and functional imaging of breast cancer. *Cancer Control* **17**, 143–155 (2010).
6. A. Berriolo-Riedinger, S. Becker, O. Casasnovas, T. Vander Borght, V. Édeline, Role of FDG PET-CT in the treatment management of Hodgkin lymphoma. *Cancer Radiother.* **22**, 393–400 (2018).
7. V. Ntziachristos, M. A. Pleitez, S. Aime, K. M. Brindle, Emerging technologies to image tissue metabolism. *Cell Metab.* **29**, 518–538 (2019).
8. M. Gallach, M. Mikhail Lette, M. Abdel-Wahab, F. Giammarile, O. Pellet, D. Paez, Addressing global inequities in positron emission tomography-computed tomography (PET-CT) for cancer management: A statistical model to guide strategic planning. *Med. Sci. Monit.* **26**, e926544 (2020).
9. OECD, "Health Care Utilisation: Diagnostic Exams" (2020); https://stats.oecd.org/Index.aspx?&datasetcode=HEALTH_PROC.
10. M. S. Linet, T. L. Slovis, D. L. Miller, R. Kleinerman, C. Lee, P. Rajaraman, A. Berrington de Gonzalez, Cancer risks associated with external radiation from diagnostic imaging procedures. *CA Cancer J. Clin.* **62**, 75–100 (2012).
11. A. Kaushik, A. Jaimini, M. Tripathi, M. D. Souza, R. Sharma, A. Mondal, A. K. Mishra, B. S. Dwarakanath, Estimation of radiation dose to patients from 18 FDG whole body PET / CT investigations using dynamic PET scan protocol. *Indian J. Med. Res.* **142**, 721–731 (2015).
12. N. Anan, R. Zainon, M. Tamal, A review on advances in ^{18}F-FDG PET/CT radiomics standardisation and application in lung disease management. *Insights Imaging* **13**, 22 (2022).
13. H. M. De Feyter, K. L. Behar, Z. A. Corbin, R. K. Fulbright, P. B. Brown, S. McIntyre, T. W. Nixon, D. L. Rothman, R. A. de Graaf, Deuterium metabolic imaging (DMI) for MRI-based 3D mapping of metabolism in vivo. *Sci. Adv.* **4**, eaat7314 (2018).
14. O. Warburg, On respiratory impairment in cancer cells. *Science* **124**, 269–270 (1956).
15. O. Warburg, On the origin of cancer cells. *Science* **123**, 309–314 (1956).
16. G. D. Mateescu, A. Ye, C. A. Flask, B. Erokwu, J. L. Duerk, In vivo assessment of oxygen consumption via deuterium magnetic resonance. *Adv. Exp. Med. Biol.* **701**, 193–199 (2011).
17. R. Mahar, P. L. Donabedian, M. E. Merritt, HDO production from [$^2H_7$]glucose quantitatively identifies warburg metabolism. *Sci. Rep.* **10**, 8885 (2020).
18. R. Mahar, H. Zeng, A. Giacalone, M. Ragavan, T. H. Mareci, M. E. Merritt, Deuterated water imaging of the rat brain following metabolism of [$^2H_7$]glucose. *Magn. Reson. Med.* **85**, 3049–3059 (2021).
19. R. Mahar, M. C. Chang, M. E. Merritt, Measuring NQO1 Bioactivation Using [2H7]Glucose. *Cancer* **13**, 4165 (2021).
20. G. M. Fischer, Y. N. Vashisht Gopal, J. L. McQuade, W. Peng, R. J. DeBerardinis, M. A. Davies, Metabolic strategies of melanoma cells: Mechanisms, interactions with the tumor microenvironment, and therapeutic implications. *Pigment Cell Melanoma Res.* **31**, 11–30 (2018).

21. K. Meeth, J. X. Wang, G. Micevic, W. Damsky, M. W. Bosenberg, The YUMM lines: a series of congenic mouse melanoma cell lines with defined genetic alterations. *Pigment Cell Melanoma Res.* **29**, 590–597 (2016).
22. H. Yang, D. A. Kircher, K. H. Kim, A. H. Grossmann, M. W. VanBrocklin, S. L. Holmen, J. P. Robinson, Activated MEK cooperates with Cdkn2a and Pten loss to promote the development and maintenance of melanoma. *Oncogene* **36**, 3842–3851 (2017).
23. A. Carracedo, P. P. Pandolfi, The PTEN–PI3K pathway: Of feedbacks and cross-talks. *Oncogene* **27**, 5527–5541 (2008).
24. A. Papa, P. P. Pandolfi, The PTEN–PI3K axis in cancer. *Biomolecules* **9**, 153 (2019).
25. A. Carnero, J. M. Paramio, The PTEN/PI3K/AKT Pathway in vivo. *Cancer Mouse Models. Front. Oncol.* **4**, (2014).
26. C. Farah, M.-A. Neveu, C. Yelek, C. Bouzin, B. Gallez, J.-F. Baurain, L. Mignion, B. F. Jordan, Combined HP ^{13}C pyruvate and 13C-glucose fluxomic as a potential marker of response to targeted therapies in YUMM1.7 melanoma xenografts. *Biomedicines* **10**, 717 (2022).
27. T. J. Parmenter, M. Kleinschmidt, K. M. Kinross, S. T. Bond, J. Li, M. R. Kaadige, A. Rao, K. E. Sheppard, W. Hugo, G. M. Pupo, R. B. Pearson, S. L. McGee, G. V. Long, R. A. Scolyer, H. Rizos, R. S. Lo, C. Cullinane, D. E. Ayer, A. Ribas, R. W. Johnstone, R. J. Hicks, G. A. McArthur, Response of BRAF-mutant melanoma to BRAF inhibition is mediated by a network of transcriptional regulators of glycolysis. *Cancer Discov.* **4**, 423–433 (2014).
28. C. Robert, B. Karaszewska, J. Schachter, P. Rutkowski, A. Mackiewicz, D. Stroiakovski, M. Lichinitser, R. Dummer, F. Grange, L. Mortier, V. Chiarion-Sileni, K. Drucis, I. Krajsova, A. Hauschild, P. Lorigan, P. Wolter, G. V. Long, K. Flaherty, P. Nathan, A. Ribas, A.-M. Martin, P. Sun, W. Crist, J. Legos, S. D. Rubin, S. M. Little, D. Schadendorf, Improved overall survival in melanoma with combined dabrafenib and trametinib. *N. Engl. J. Med.* **372**, 30–39 (2015).
29. A. Tasdogan, B. Faubert, V. Ramesh, J. M. Ubellacker, B. Shen, A. Solmonson, M. M. Murphy, Z. Gu, W. Gu, M. Martin, S. Y. Kasitinon, T. Vandergriff, T. P. Mathews, Z. Zhao, D. Schadendorf, R. J. DeBerardinis, S. J. Morrison, Metabolic heterogeneity confers differences in melanoma metastatic potential. *Nature* **577**, 115–120 (2020).
30. V. Di Gialleonardo, S. S. Tee, H. N. Aldeborgh, V. Z. Miloushev, L. S. Cunha, G. D. Sukenick, K. R. Keshari, High-throughput indirect quantitation of ^{13}C enriched metabolites using ^{1}H NMR. *Anal. Chem.* **88**, 11147–11153 (2016).
31. F. Niess, B. Strasser, L. Hingerl, E. Niess, S. Motyka, G. Hangel, M. Krššák, S. Gruber, B. Spurny-Dworak, S. Trattnig, T. Scherer, R. Lanzenberger, W. Bogner, Reproducibility of 3D MRSI for imaging human brain glucose metabolism using direct (^{2}H) and indirect (^{1}H) detection of deuterium labeled compounds at 7T and clinical 3T. *Neuroimage* **277**, 120250 (2023).
32. J. D. Kaggie, A. S. Khan, T. Matys, R. F. Schulte, M. J. Locke, A. Grimmer, A. Frary, I. H. Menih, E. Latimer, M. J. Graves, M. A. McLean, F. A. Gallagher, Deuterium metabolic imaging and hyperpolarized ^{13}C-MRI of the normal human brain at clinical field strength reveals differential cerebral metabolism. *Neuroimage* **257**, 119284 (2022).
33. P. M. Adamson, K. Datta, R. Watkins, L. D. Recht, R. E. Hurd, D. M. Spielman, Deuterium metabolic imaging for 3D mapping of glucose metabolism in humans with central nervous system lesions at 3T. *Magn. Reson. Med.* **91**, 39–50 (2024).
34. A. S. Khan, K. A. Peterson, O. I. Vittay, M. A. McLean, J. D. Kaggie, J. T. O'Brien, J. B. Rowe, F. A. Gallagher, T. Matys, S. Wolfe, Deuterium metabolic imaging of alzheimer disease at 3-T magnetic field strength: A pilot case-control study. *Radiology* **312**, e232407 (2024).
35. J. P. Nolan, "Anaesthesia and neuromuscular block," in *Clinical Pharmacology* (Elsevier, 2012), pp. 295–310; https://linkinghub.elsevier.com/retrieve/pii/B9780702040849000586.
36. H. J. Koch, R. S. Stuart, The synthesis of per-C-deuterated D-glucose11 Presented at the 2nd Joint CIC-ACS Conference, Montreal, Quebec, Canada, June 1, 1977. *Carbohydr. Res.* **64**, 127–134 (1978).
37. C. Zou, Y. Ruan, H. Li, Q. Wan, F. Du, J. Yuan, Q. Qin, G. J. Thompson, X. Yang, Y. Li, X. Liu, H. Zheng, A new deuterium-labeled compound [2,3,4,6,6′- $^{2}H_5$]-D-glucose for deuterium magnetic resonance metabolic imaging. *NMR Biomed.* **36**, e4890 (2023).
38. L. Ruhm, T. Ziegs, A. M. Wright, C. S. Mathy, S. Murali-Manohar, J. Dorst, N. Avdievich, A. Henning, Dynamic observation of ^{2}H labeled compounds in the human brain with ^{1}H versus ^{2}H magnetic resonance spectroscopy at 9.4T. *bioRxiv* 2022.01.24.477582 , (2022).
39. H. Asano, A. E. Elhelaly, F. Hyodo, R. Iwasaki, Y. Noda, H. Kato, K. Ichihashi, H. Tomita, M. Murata, T. Mori, M. Matsuo, Deuterium magnetic resonance imaging using deuterated water-induced ^{2}H-tissue labeling allows monitoring cancer treatment at clinical field strength. *Clin. Cancer Res.* **29**, 5173–5182 (2023).
40. M. McLeod, M. C. Chang, A. Rushin, M. Ragavan, R. Mahar, G. Sharma, A. Badar, A. Giacalone, M. E. Glanz, V. R. Malut, D. Graham, N. E. Sunny, J. A. Bankson, K. Cusi, M. E. Merritt, Detecting altered hepatic lipid oxidation by MRI in an animal model of MASLD. *Cell Rep. Med.* **5**, 101714 (2024).
41. E. T. Montrazi, K. Sasson, L. Agemy, D. C. Peters, O. Brenner, A. Scherz, L. Frydman, High-sensitivity deuterium metabolic MRI differentiates acute pancreatitis from pancreatic cancers in murine models. *Sci. Rep.* **13**, 19998 (2023).
42. F. Hesse, A. J. Wright, V. Somai, F. Bulat, F. Kreis, K. M. Brindle, Imaging glioblastoma response to radiotherapy using ^{2}H magnetic resonance spectroscopy measurements of fumarate metabolism. *Cancer Res.* **82**, 3622–3633 (2022).
43. D. C. Peters, S. Markovic, Q. Bao, D. Preise, K. Sasson, L. Agemy, A. Scherz, L. Frydman, Improving deuterium metabolic imaging (DMI) signal-to-noise ratio by spectroscopic multi-echo bSSFP: A pancreatic cancer investigation. *Magn. Reson. Med.* **86**, 2604–2617 (2021).
44. G. Zhang, Q. Cullen, M. Berishaj, K. Deh, N. Kim, K. R. Keshari, [6,6′- $^{2}H_2$] fructose as a deuterium metabolic imaging probe in liver cancer. *NMR Biomed.* **36**, e4989 (2023).
45. L. M. Zopf, P. Heimel, S. H. Geyer, A. Kavirayani, S. Reier, V. Fröhlich, A. Stiglbauer-Tscholakoff, Z. Chen, L. Nics, J. Zinnanti, W. Drexler, M. Mitterhauser, T. Helbich, W. J. Weninger, P. Slezak, A. Obenauf, K. Bühler, A. Walter, Cross-modality imaging of murine tumor vasculature—A feasibility study. *Mol. Imaging Biol.* **23**, 874–893 (2021).
46. M. C. Chang, R. Mahar, M. A. McLeod, A. G. Giacalone, X. Huang, D. A. Boothman, M. E. Merritt, Synergistic effect of β-lapachone and aminooxyacetic acid on central metabolism in breast cancer. *Nutrients* **14**, 3020 (2022).
47. R. Mahar, M. Ragavan, M. C. Chang, S. Hardiman, N. Moussatche, A. Behar, R. Renne, M. E. Merritt, Metabolic signatures associated with oncolytic myxoma viral infections. *Sci. Rep.* **12**, 12599 (2022).
48. S. J. Staklinski, M. C. Chang, F. Yu, K. Collins Ruff, D. N. Franz, Z. Qian, L. B. Bloom, M. E. Merritt, R. McKenna, M. S. Kilberg, Cellular and molecular characterization of two novel asparagine synthetase gene mutations linked to asparagine synthetase deficiency. *J. Biol. Chem.* **298**, 102385 (2022).
49. M. C. Chang, S. J. Staklinski, V. R. Malut, G. L. Pierre, M. S. Kilberg, M. E. Merritt, Metabolomic profiling of asparagine deprivation in asparagine synthetase deficiency patient-derived cells. *Nutrients* **15**, 1938 (2023).
50. J. D. Young, INCA: A computational platform for isotopically non-stationary metabolic flux analysis. *Bioinformatics* **30**, 1333–1335 (2014).
51. M. Rahim, M. Ragavan, S. Deja, M. E. Merritt, S. C. Burgess, J. D. Young, INCA 2.0: A tool for integrated, dynamic modeling of NMR- and MS-based isotopomer measurements and rigorous metabolic flux analysis. *Metab. Eng.* **69**, 275–285 (2022).
52. H. Gudbjartsson, S. Patz, The Rician distribution of noisy MRI data. *Magn. Reson. Med.* **34**, 910–914 (1995).

Acknowledgments: A portion of this work was performed in the McKnight Brain Institute at the National High Magnetic Field Laboratory's Advanced Magnetic Resonance Imaging and Spectroscopy (AMRIS) Facility, which is supported by National Science Foundation Cooperative agreement nos. DMR-2128556 and DMR-1644779 and the State of Florida. **Funding:** The research presented was made possible by the following sources of funding: National Institutes of Health grants R01-EB032376 (to M.E.M., V.D.K., J.A.B.) and grant R01-DK132254 (to M.E.M.). **Author contributions:** Writing—original draft: M.C.C., G.L.P., and M.E.M. Conceptualization: M.C.C., V.R.M., G.L.P., M.R., A.D.R., R.J.D., and M.E.M. Investigation: M.C.C., V.R.M., R.M., A.R., M.A.M., G.L.P., S.J.S., M.E.G., M.R., G.S., M.M., A.B., M.S.K., V.D.K., J.A.B., and R.J.D. Writing—review and editing: M.C.C., V.R.M., R.M., A.R., M.A.M., S.J.S., M.E.G., A.D.R., B.K.L., M.S.K., V.D.K., J.A.B., R.J.D., and M.E.M. Methodology: M.C.C., V.R.M., R.M., A.R., M.A.M., S.J.S., M.E.G., M.R., A.D.R., R.J.D., and M.E.M. Resources: S.J.S., M.R., M.S.K., and R.J.D. Funding acquisition: M.S.K., V.D.K., J.A.B., and M.E.M. Data curation: M.C.C., V.R.M., and R.M. Validation: M.C.C., V.R.M., R.M., A.R., M.A.M., G.L.P., S.J.S., G.S., M.S.K., and M.E.M. Supervision: B.K.L., M.S.K., V.D.K., J.A.B., R.J.D., and M.E.M. Formal analysis: M.C.C., R.M., I.R.M., S.J.S., M.S.K., and M.E.M. Software: M.C.C., V.R.M., M.R., M.A.M., J.H.P.C., V.D.K., J.A.B., and M.E.M. Project administration: M.S.K. and M.E.M. Visualization: M.C.C., R.M., I.R.M., S.J.S., and M.E.M. **Competing interests:** M.E.M. and R.M. are inventors on US patent no. 17906508 held by the University of Florida, which pertains to HDO metabolic imaging (patent assigned on 22 December 2023). R.J.D. receives consulting fees from Atavistik Bio, Agios Pharmaceuticals, Vida Ventures, and Droia Ventures. R.J.D. is a founder and advisor at Atavistik Bio and serves on the scientific advisory boards of Agios Pharmaceuticals and Vida Ventures. All other authors declare that they have no competing interests. **Data and materials availability:** All data needed to evaluate the conclusions in the paper are present in the paper and/or the Supplementary Materials.

Submitted 14 June 2024
Accepted 24 February 2025
Published 26 March 2025
10.1126/sciadv.adr0568